Author/s:
Roy, A;O'Loughlin, CD;Chow, SH;Randolph, MF

Title:
Inclined loading of horizontal plate anchors in sand

Date:
2022-12-01

Citation:
Roy, A., O'Loughlin, C. D., Chow, S. H. & Randolph, M. F. (2022). Inclined loading of horizontal plate anchors in sand. Geotechnique, 72 (12), pp.1051-1067. https://doi.org/10.1680/jgeot.20.P.119.

Persistent Link:
https://hdl.handle.net/11343/279371

Inclined loading of horizontal plate anchors in sand

A. Roy[1], C.D. O'Loughlin[2], S.H Chow[3], M.F. Randolph[4]

[1,2,4] Centre for Offshore Foundation Systems, University of Western Australia, Australia

[3] Department of Infrastructure Engineering, the University of Melbourne, Australia

Article manuscript submitted to Gèotechnique

First submission: April 2020

[1]Corresponding Author
PhD student, Centre for Offshore Foundation Systems (BEng, MEng)
The University of Western Australia
35 Stirling Highway, Crawley WA 6009, Perth, Australia
E-mail: anamitra.roy@research.uwa.edu.au
Orcid: (0000-0002-3093-1848)

[2]Associate Professor, Centre for Offshore Foundation Systems (BEng, PhD)
The University of Western Australia
35 Stirling Highway, Crawley WA 6009, Perth, Australia
Phone: +61 8 6488 6488
E-mail: conleth.oloughlin@uwa.edu.au
Orcid: (0000-0002-5823-6265)

[2]Senior Lecturer, Department of Infrastructure Engineering (BEng, MEng, PhD)
Engineering Block B, Grattan Street, Parkville
The University of Melbourne, Victoria 3010, Australia
Phone: +61 3 9035 7504
E-mail: shiaohuey.chow@unimelb.edu.au
Orcid: (0000-0002-5442-0014)
Formerly Centre for Offshore Foundation Systems, The University of Western Australia

[4]Professor, Centre for Offshore Foundation Systems (MA, PhD, FAA, FREng, FRS, FTSE, FIEAust, CPEng)
The University of Western Australia
35 Stirling Highway, Crawley WA 6009, Perth, Australia
Phone: +61 8 6488 3075
E-mail: mark.randolph@uwa.edu.au

Number of words	6615 (excluding abstract, references and captions)
Number of figures	17
Number of tables	06

Inclined loading of horizontal plate anchors in sand

A. Roy[1], C.D. O'Loughlin [2], S.H Chow [3], M.F. Randolph[4]

[1,2,4] Centre for Offshore Foundation Systems, University of Western Australia, Australia

[3] Department of Infrastructure Engineering, the University of Melbourne, Australia

Abstract

The performance of plate anchors in sand, relative to clay, is not well understood, particularly for the more realistic case of an inclined load. This paper investigates the effect of load inclination on horizontal plate anchors in sand through centrifuge tests and numerical finite element (FE) simulations. The centrifuge tests were performed using rectangular plate anchors in loose and dense sand, at shallow embedment depths with four different load inclinations. The experiments showed that anchor capacity of horizontal plates increased progressively as the load inclination became progressively more horizontal, with anchor capacity under pure horizontal loading being approximately 1.8 times higher than that under pure vertical loading. These experimental observations were also replicated in finite element simulations using a bounding surface plasticity model. Investigation of the underlying failure mechanisms and stress paths showed that the slip planes become longer and the mobilised lateral stresses increase as the load inclination becomes increasingly horizontal, which leads to higher anchor capacities. Finally, the anchor resistance factors from the numerical probe analyses were decoupled into vertical and horizontal components and represented as interaction diagrams, providing a basis for performing hand calculations of anchor capacity for a given embedment depth, load inclination and relative density.

Keywords

Plate anchors; inclined loading; bounding surface plasticity; interaction diagram; finite element analysis; sands

List of notations

δ	Anchor displacement
δ_{soil}	Soil displacement
$\Delta\gamma_{oct}^{p}$	Incremental octahedral plastic shear strain
γ'	Effective unit weight of soil
θ	Load inclination for plate anchor

ϕ_c	Critical state friction angle
ϕ_{ds}	Direct shear friction angle
ϕ	Soil friction angle
θ_l	Lode angle
ψ	State parameter
A	Area of the plate anchor
a_1, a_2, a_3	Constants for the interaction diagram
B	Plate anchor width
d_{50}	The median particle size of the sand
F_c, F_m	Measured load and corrected load on plate anchor
F_H, F_V	Horizontal and vertical reaction forces on the anchor plate
g	Centrifuge acceleration levels
H	Embedment depth to the top of the anchor plate
j	Fitting constant
K_0	Coefficient of earth pressure
L	Plate anchor length
M	Mobilised stress ratio
N_γ	Anchor factor
$N_{\gamma,H}$, $N_{\gamma,V}$	Horizontal and vertical components of anchor resistance factors
$N_{\gamma,V(\theta = 0°)}$	vertical anchor resistance factor at $\theta_l = 0°$
P_a	Atmospheric pressure
p'	Mean effective stress
q	Deviatoric stress on a soil element
q_c	Cone tip resistance
R_D	Relative density
R_n	Average normalised roughness for plate anchor model
R_{max}	Maximum peak-to-valley distance over 2.5 mm reference length on a rigid body
RP	Reference point
s_1, s_2, s_3	Principal components of the deviatoric stress tensor
S_f	Shape factor
t	Thickness of plate anchor model used in experiments
U	Uniformity coefficient of sand
z	Vertical depth

Introduction

Plate anchors are being considered increasingly for offshore renewable energy applications such as floating wave energy devices (e.g. Gaudin et al. 2017) and floating offshore wind turbines (Hallowell et al. 2018, Fontana et al. 2016). As these developments are typically sited in relative shallow water (e.g. < 100 m) where the seabed is more likely to be coarse grained (Chow et al. 2018a), their performance in sandy seabeds is of interest. Although well-studied in clay (O'Neill et al. 2003, Yang et al. 2010), plate anchors in sand have received minimal attention, particularly for realistic loading cases where the anchor is inclined and the load is at an angle that is less than normal to the plate (see Fig. 1).

The majority of the research effort into understanding the behaviour of plate anchors in sand has focused on either a vertical plate anchor subjected to horizontal loading (Fig. 1(a)) (Merifield & Sloan 2006, Choudhary & Dash 2013, Kumar & Sahoo 2012) or a horizontal plate anchor subjected to vertical loading (Fig. 1 (b)), (Smith 2012, White et al. 2008, Sakai & Tanaka 2007, Bhattacharya & Kumar 2014, Han 2016). These investigations have identified typical failure mechanism for the two loading cases and have led to empirical approaches for estimating anchor capacity through the use of mobilized friction and dilation angles.

Relative to the above cases, evaluating anchor capacity and the associated failure mechanism for an inclined plate subjected to an inclined load (Fig. 1(c) and Fig. 1(d)) is markedly more complex. This is because the distance from the anchor to the free surface along the direction of loading varies, resulting in uncertainties in predicting anchor capacity due to:

- potential variation of the governing factors controlling anchor uplift, such as passive resistance of the mobilised influence zone and the shearing forces on the slip planes;
- predominantly inclined direction of interaction of the major principal stress in the influence zone with the possible horizontal bedding anisotropy of the soil; and
- simultaneous mobilisation of normal and shear reactions on the plate, giving rise to a complex interplay of bearing and shearing dominated mechanisms.

In light of this, the uncertainty in predicting plate anchor capacity under an inclined loading in coarse-grained soils needs to be addressed. Attention also needs to be given to identification of the governing mechanisms at peak load conditions under different loading inclinations, quantifying friction angles associated with the different stress paths, which may then be applied in more routine design approaches.

This paper addresses the knowledge gap on inclined loading described above through centrifuge experiments and finite element (FE) simulations. The investigation focuses specifically on inclined loading of a horizontal anchor (Fig. 1(d)), as it creates a basis for observing the gradual change in the of governing mechanisms as the loading inclination changes, and serves as a necessary intermediate step in the quest for a generalised interaction diagram for inclined anchors.

The experiments encompassed both loose and dense sand states, three different anchor embedment ratios, and four different loading inclinations. The problem was also investigated through FE analyses using a sophisticated bounding surface plasticity model that takes into account the variation of dilation with relative density, mean stress (elaborated in Dafalias et al. 2004, Dafalias & Manzari 2004 and Papadimitriou et al. 2005) with some practical modifications to allow for more realistic modelling of anisotropy. The present work did not implement the more complex variations to the model that have been introduced to account for cyclic loading reversals and stress rotations over multiple cycles (e.g. Li & Dafalias (2012) and Petalas et al. (2019)). The FE analysis aims to provide further understanding of the underlying failure mechanisms and governing stress paths under inclined loading. The results considering different loading angles were then used to develop interaction diagrams that were fitted by simple algebraic equations for use in design.

Experimental details

Model setup details

The centrifuge experiments were conducted at 20*g* using stainless steel plate anchors of width B = 30 mm, length L = 60 mm and thickness t = 5 mm. Surface roughness was quantified from profilometer measurements (with a stylus tip radius of 2 μm), which gave an average normalised roughness $R_n = R_{max}/d_{50}$ = 0.1 (where R_{max} is the maximum peak-to-valley distance over an 2.5 mm reference length and d_{50} is the median particle size of the sand used in the experiments; see Table 1) allowing the plate anchor interface to be considered fully rough (Paikowsky et al. 1995), or close to fully rough (Lings and Dietz, 2005).

The anchors were loaded using a two directional electrical actuator (located on the surface of the sample container) at load inclinations, θ = 0°, 30°, 60° and 90° (to the vertical) as shown in Fig. 2. Vertical loading (θ = 0°) was achieved using a smooth rod, 4.7 mm in diameter, screwed to the centre of the plate. The rod extended to above the sand surface, such that it was accessible to the actuator, creating a means of loading the plate anchor (see Fig. 3(a)). Horizontal loading (θ = 90°) used a 1.6 mm diameter Kevlar line that connected the mid-height of the anchor to the actuator. The Kevlar line passed under a rod located at the side of the sample container, and positioned such that the Kevlar line was horizontal (see Fig. 3(c) and also Chow et al. 2018b). For the inclined loading tests (θ = 30° or 60°), a bridle was created using four 0.6 mm diameter Kevlar lines that connected to a 1.6 mm diameter Kevlar loading line at an attachment point located 15 mm above the plate (Fig. 2(d)). The length of the bridle lines was selected such that when taut, the load was inclined at either θ = 30° or 60°; i.e. the line of action of the load was through the geometric centre of gravity of the plate, preventing moment development on the plate and rotation. Maintaining this load inclination during the inclined loading tests was achieved using a pulley located at the base of the actuator, and positioned at a pre-determined location to achieve the desired inclination, as shown in Fig. 3(b). Verification that this procedure resulted in no rotation of the anchor during loading was obtained from a series of trial centrifuge tests where the anchor was carefully exposed by vacuuming the sand above the anchor after the test to check the orientation.

Sample details

The experiments were conducted in a fine sub-angular silica sand, with properties as summarised in Table 1. Six dry sand samples were prepared to target two relative densities (R_D ~ 45% and ~70%) and three anchor embedment depths. The distance H from the sand surface to the top of the plate was either 55 mm, 85 mm or 115 mm, giving plate embedment ratios (H/B) of 1.83, 2.83 and 3.83 respectively. Four anchor tests were conducted in each sample at the four load inclinations at a specific anchor embedment ratio and sand density (Fig. 4).

The sand samples were prepared in rectangular centrifuge sample containers (or 'strongboxes') with internal dimensions of 650 mm × 390 mm × 325 mm (length × width × height) by air pluviation. To eliminate potential anchor installation effects – which are not the focus of this study – the anchors were pre-embedded in the samples (analogous to 'wished-in-place' in numerical modelling). This was achieved by pausing pluviation when the sand reached the required anchor embedment depth, vacuum levelling the sand surface and careful placement of the anchors and any ancillary equipment such as that needed for the horizontally loaded anchor (see Fig. 4). For the inclined loading cases, the loading lines were tied to a grid of 0.6 mm diameter Kevlar wires above the strongbox, positioned to achieve the required load inclination (see Fig. 4). Pluviation was then resumed and the sample surface of the sample was vacuum levelled to achieve final sample heights of 180 mm, 210 mm and 240 mm for samples that investigated embedment ratios of H/B of 1.83, 2.83 and 3.83 respectively. The grid of

Kevlar wires above the strongbox was subsequently removed and the loading line for the anchor to be tested was connected to the actuator, via an in-line load cell, before spinning the centrifuge to the testing acceleration of 20g.

Cone penetrometer tests (CPTs) were conducted in each sample, using a 10 mm diameter cone penetrometer, both before and after the anchor tests. Depth profiles of cone tip resistance (q_c) with depth (z) are provided in Fig. 5, showing the expected increase in cone resistance with depth, reflecting the dependence of q_c on vertical effective stress level. Determining relative density from global measurements of sample mass and volume was hindered by inclusion of the plate anchors in the sample. For this reason, relative density (and subsequently unit weight) was determined from the empirical relationship between cone tip resistance (q_c) and relative density (R_D) proposed by Roy et al. (2019) for UWA silica sand. These profiles (also shown in Fig. 5) indicate that relative density at the anchor locations was typically in the range R_D = 41 – 51% and R_D = 69 – 76% in the loose and dense samples respectively, consistent with the targeted R_D = 45% and R_D = 70%. The profiles were determined both before and after the anchor tests, and indicate that the samples densified slightly over the course of the testing. Similar observations were reported in the centrifuge studies reported by Chow et al. (2018c) and Roy et al. (2019), and are attributed to slight densification caused by the numerous spin up/down cycles associated with centrifuge testing. The q_c and R_D profiles also indicate that whilst the three dense samples appear to be at a similar density state, the loose sample 4_L (for the tests at H/B = 3.83, see Table 2) was looser than the other loose samples (2_L and 3_L for the tests at H/B = 1.83 and 2.83 respectively, see Table 2), which as discussed later in the paper has some implications for the tests conducted in sample 4_L. The unit weight (γ) for each sample was taken as the average value obtained from the CPT responses before and at the end of testing, as summarised in Table 2.

Experimental results

The variation in anchor capacity across the different tests is evident in Fig. 6, which plots the anchor resistance factor ($N_\gamma = F_c/A\gamma'H$) against normalised anchor displacement (δ/B for θ = 0°) or mooring line displacement (δ_l/B) (for θ = 30°, 60°, 90°) in loose and dense sand samples respectively. The measured loads (F_m in Table 2) were corrected to obtain F_c by deducting the vertical component of anchor weight for the different load inclinations and, for the θ = 90° case only, the estimated friction loss as the loading line wraps around the horizontal rod that maintained the horizontal load inclination (see Fig. 3 and Fig. 4). The latter correction for friction amounted to ~9.8% of the measured resistance, calculated by assuming a kinetic friction coefficient of 0.065 (therefore, as per the belt friction equation for this case, $F_c/F_m = e^{-0.065\,\pi/2}$). Fig. 6 shows that anchor capacity increases with increasing load inclination (i.e. as the load direction becomes increasingly horizontal), increasing relative density and increasing embedment. The distance required to mobilise peak anchor capacity also increases with increasing load inclination and with increasing anchor embedment. Although an amount of the anchor displacement reported in Fig. 6 is due to recovery of slack in the mooring line, higher mobilisation distances are to be expected at the higher load inclinations, consistent with differing mobilisation rates for frictional and passive resistances.

Anchor capacities for load inclinations of θ = 30° and θ = 60° are higher by factors of approximately 1.13 and 1.35 respectively, than for purely vertical loading (θ = 0°). As load inclination increases to θ = 90° (i.e. horizontal loading), anchor capacity becomes approximately 1.85 and 1.7 times higher (at H/B = 1.83 and 2.83 respectively) than for pure vertical loading. These relative increases are significantly lower than those reported by Chow et al. (2018b) from single gravity experiments, where the corresponding ratios ranged between 2.0 and 4.7 for the same sand. The disparity may be due to possible effects of higher dilation at the much lower stress levels in the single gravity experiments.

As the experiments were designed to prevent rotation of the plate, the kinematic trajectory of the plate coincided with the direction of loading, forcing consistent failure kinematics of the anchor. As such, the vertical ($N_{\gamma,V}$) and horizontal ($N_{\gamma,H}$) components of the anchor resistance factor (N_γ) may be resolved from simple trigonometry and represented on the interaction diagram shown in Fig. 7. Overall, the shape of the interaction diagram is remarkably consistent across the different embedment ratios, load inclinations and densities, albeit that the tests in loose sand at H/B = 3.83 turned out to be very close to those at H/B = 2.83. As noted earlier in the paper, this was because R_D was slightly lower in this sample (see Table 2), with q_c at H/B = 3.83 in sample 4_L almost identical to q_c at H/B = 2.83 in sample 3_L.

As the interaction diagram is relatively flat for load inclinations up to θ = 60°, there is little interaction between the vertical and horizontal components of capacity over this range of load inclinations. An interesting feature of the interaction diagrams on Fig. 7 is the negative gradient in the vicinity of the $N_{\gamma,H}$ axis. This suggests that the ultimate horizontal capacity would occur at a negative value of $N_{\gamma,V}$, i.e. under a compressive vertical load.

This behaviour under pure horizontal loading (θ = 90°) is also markedly different from that in clay (Yang et al. 2010), where $N_{\gamma,H}$ is governed by pure friction at the clay-anchor interfaces and attains a value of approximately 2.0. If a similar exercise was adopted for a negligibly thin rough plate anchor in sand, with $N_{\gamma,H}$ =

2 tan(δ) (where δ is the interface friction angle, taken as the peak friction angle, ϕ = 39.7° for R_D ~50% and ϕ = 44.7° for R_D ~ 70% determined from Bolton's (1986) correlations at the respective in-situ stress levels), values of $N_{\gamma,H}$ = 1.62 and 1.97 would be obtained for R_D = 45% and 70% respectively. These values would correspond to only around 30 to 40% of the measured values, suggesting that additional resistance in this case is due to:

- shearing within the soil mass rather than at the plate-sand interface. This phenomenon of shearing within the sand (referred to as a dilative interface in Dove & Jarrett (2002)) is consistent with results from interface friction tests at similar sand densities (e.g. Uesugi & Kishida 1986).
- a contribution of bearing resistance at the anchor edges.

The relative contribution of these two factors is expected to vary with plate embedment depth and relative density, and is difficult to quantify using analytical calculations for anchor capacity. However, both contributions are captured in the numerical simulations as shown in the following sections.

Numerical methodology

A series of finite element (FE) analyses were undertaken to provide further insights into the behaviour observed in the centrifuge tests, and to allow for examination over a wider parametric space. Rather than simulating the rectangular plate anchors used in the centrifuge experiments, the numerical analyses considered a strip anchor (with t/B = 0.1) at the same embedment ratios (H/B) and (approximately the same) relative densities as in the experiments. This avoided the need for a 3D FE model, which would have been computationally challenging, and unwarranted as the motivation for the FE analyses was to understand behaviour rather than matching the responses measured in the experiments closely.

Details of the numerical analysis

The problem was modelled numerically in Abaqus (Dassault Systemes, 2012) using a series of displacement controlled, plane strain analysis, with an unstructured mesh composed of linear quadrilateral elements (CPE4). The anchor was defined as weightless and fully rigid, with its centre taken as the reference point (*RP*) for the application of displacements (Fig. 8). The corners of the anchor in contact with the soil were filleted with a radius of 0.02B to avoid numerical convergence issues. The analyses were conducted for an anchor plate width (B) of 1 m and thickness (t) of 0.1B at shallow embedment ratios (H/B = 2, 3, 4) in sand of relative densities (R_D) of 30%, 50% and 70%. The interaction diagram in V-H space was constructed by conducting displacement probes at inclinations (θ) of 0°, 15°, 30°, 60°, 75° and a few discrete values between 80° and 85° rather than 90°, due to difficulties in obtaining convergence for θ = 90°. As evident in Fig. 8, the bottom boundary of the soil domain was fixed at a distance of 3*B* below the anchor base, whereas the lateral boundary was increased from 5*B* to 11*B* as the load inclination and embedment increased. All nodes on the bottom boundary were fully restrained, whereas lateral restraint only was imposed for nodes on the side boundaries.

Experimental investigations on shallowly embedded horizontal plate anchors and pipes under drained vertical loading conditions have shown that the base of the plate or pipe is expected to separate from the underlying soil within displacements levels of 5% of the pipe diameter or plate width (Liu et al. 2012). However, previous numerical studies suggest that the capacity of horizontal plate anchors loaded vertically is not influenced by interface conditions (Merifield & Sloan 2006, Hao et al. 2014), particularly because the effective stress in the sand underneath the plate becomes very low and does not contribute to shear strength. Trial simulations for both loose and dense sand states and at embedment ratios up to H/B = 4 indicated differences in anchor capacity by less than 1% when separation was allowed at the underside of the anchor, with convergence difficulties arising at higher embedment depths. Hence, the soil-anchor interface was taken as fully rough with no separation allowed during loading.

Constitutive model and its implementation for the FE analysis

The bounding surface constitutive platform adopted in the FE simulations is similar to that proposed by Dafalias & Manzari (2004) (with cyclic variables kept dormant) or Dafalias et al. (2004) as it embraces typical bounding surface plasticity features with kinematic hardening. The dilatancy and bounding surfaces in the model are expressed as a function of the state parameter (ψ); this unifies the treatment of loose and dense sands under one constitutive framework and also allows the surfaces to collapse on to the critical state as ψ approaches zero, thus simulating stress and volume constancy at critical state. Some minor practical modifications pertaining to the treatment of fabric anisotropy were introduced through scaling factors to adjust the influence of ψ on the model's governing equations (see Eqn. (24) to (26) in Table 3) for realistic performance over different monotonic loading directions, namely triaxial compression, extension and simple shear. The explicit incorporation of fabric anisotropy based on loading direction and fabric orientation (through the term A_{ratio} in Eq. (23)) makes it better suited to capture the effects of inclined loading on the soil fabric for the current problem.

The role of each of the model parameters and their calibration are summarised in Table 3. The calibrated model parameters are listed in Table 4, as determined from element tests on the same UWA silica sand used in the centrifuge experiments. Roy et al. (2020) shows the performance of the model (using the parameters listed in

Table 4) in describing the responses measured in triaxial tests and in centrifuge experiments of surface and buried foundations subjected to vertical compressive loading and demonstrates the importance of macroscopic incorporation of fabric effects in sand when analysing a boundary value problem. The soil unit weight (γ) has been assumed as 15 kN/m^3 in the numerical simulations. The coefficient of earth pressure (K_0) for the sand was taken as 0.5 and the initial position of the axis of the conical yield surface was set to coincide with the initial stress state of the soil. The maximum plate anchor incremental displacement allowed in each iteration was $0.00002B$ to maintain convergence in the global scale within two to three iterations.

Loukidis (2006), Yamamoto (2006) and Loukidis & Salgado (2011) used a softening sand constitutive model and concluded that, for a problem dominated by compressive stresses over a sufficiently large influence zone, the size of mesh elements after subsequent refinement had negligible effect on the final failure load. This is because the mobilised capacity is not influenced by the performance of a single shear band, but rather by a set of distributed shear bands in the mobilised influence zone. For the present study, results from a few preliminary analyses indicated that for $\theta < 60°$, a bearing-type mechanism distributed over an irregular trapezoidal influence zone dominates the mobilised capacity. Table 5 shows that for bearing dominated cases (i.e. $\theta = 0°$ in Table 5), N_γ converges to a constant value at a minimum soil element size of $0.025B$ when $R_D = 70\%$, and is practically constant for $R_D = 30\%$ when the minimum soil element size varies between $0.037B$ and $0.024B$. For $\theta > 60°$, the size of the elements immediately above the plate (up to ~$0.12B$) becomes more important than the total number of elements in the entire domain, as the mechanism becomes dominated by shearing (although as shown later in the paper, this shearing was within the soil and not at the soil-plate interface). As presented in Table 5 for $\theta = 85°$, N_γ converges to a constant value when the minimum soil element size reduces to the range $0.025B$ – $0.031B$. Therefore, the analyses were performed using elements with a minimum thickness of $0.02B$ – $0.023B$ for $\theta < 60°$ and with $0.019B$ – $0.027B$ for $\theta > 60°$.

Numerical results

Fig. 9 presents the load displacement responses for strip anchors at $H/B = 4$ for $R_D = 70\%$ and 30%. Anchor resistance is decoupled into horizontal and vertical anchor resistance factors, $N_{\gamma,H} = F_H/B\gamma'H$ and $N_{\gamma,V} = F_V/B\gamma'H$, where F_H amd F_V are the horizontal and vertical reaction forces developing on the plate. Vertical resistance factors are reasonably similar for both loose and dense sand states when $\theta \leq 60°$, with the initial stiff response transitioning to a plateau at a normalised displacement that increases as θ reduces. For all three values of R_D investigated, peak values of $N_{\gamma,V}$ are relatively independent of θ up to 60°, reducing by 2% as θ increases from 0° to 60° (Fig. 9(a) and Fig. 9(c)). Displacement levels associated with peak values of $N_{\gamma,V}$ depend on both θ and R_D. For example, the peak $N_{\gamma,V}$ for R_D = 70% at θ = 45° is attained at δ/B = 8%, whereas for R_D = 30%, the same is attained at δ/B ~ 10%. Previous studies (e.g. Cheuk et al. 2008, White et al. 2008) suggest that the uplift capacity is predominantly influenced by two resistance components: (a) the weight of soil above the plate and (b) shear resistance along the slip planes of the failed mechanism. The current simulations indicate that although the relative magnitude of each resistance component may change as θ varies between 0° and 60°, the underlying mechanisms governing the magnitude of $N_{\gamma,V}$ do not change appreciably (with $N_{\gamma,V}$ remaining approximately constant). In contrast, the horizontal resistance factor, $N_{\gamma,H}$, increases steadily with increasing θ (Fig. 9(b) and Fig. 9(d)).

To further examine the interaction between $N_{\gamma,H}$ and $N_{\gamma,V}$, Fig. 10 plots the variation in the ratio of (peak values of) horizontal anchor resistance factor ($N_{\gamma,H}$) to vertical anchor resistance factor at θ = 0° (i.e. $N_{\gamma,V(\theta\,=\,0°)}$) for all R_D and H/B, and as θ increases from 0° to 85°. Fig. 10 indicates that peak values of $N_{\gamma,H}$ vary linearly with load inclination up to θ = 60°, suggesting a gradual increase in inclined passive resistance with increasing load inclination. Supporting evidence is provided by the failure mechanisms (Fig. 11) from the numerical simulations.

The failure mechanisms at H/B = 4, plotted as normalised octahedral plastic shear strain contours ($\Delta\gamma^p_{oct}/\Delta\gamma^p_{oct\_max}$) along with the normalised soil displacement (δ_{soil}/δ) for three different load inclinations at peak capacity (Fig. 11), perfectly complement the simulated responses and stress paths. For θ = 0°, the plots show that the inclination of the plastic shear strain bands with the vertical (that is an approximate indication of the mobilised dilation angle) is around 15° and 5° for R_D = 70% and 30% respectively. The zones of intense shearing, emerging from the anchor edges, do not extend fully to the soil surface. The contours of normalised soil displacement (shown in red dashed lines in Fig. 11), emerging from either end of the anchor plate and reaching the soil surface, are however markedly different from the zones of intense shearing. The inclination of the displacement contour lines and their deviation from the shear bands increases towards the soil surface, as also observed in the model tests reported in Cheuk et al. (2008), which is attributed to the higher dilation as the stress reduces at shallow depths. Overall, the contours suggest that the influence zone mobilised at peak capacity is smaller for loose sand than for dense sand, regardless of load inclination. For example, at θ = 0° the width of the influence zone at the soil surface is ~4B for R_D = 30%, compared with ~5B at R_D = 70%.

As load inclination (θ) increases (say Fig. 11(c), (d)), the shear strain and displacement contours in the zone close to the anchor tend to become increasingly skewed towards the loading direction. Contrary to the observations of a single prominent shear band for θ = 0°, there is some indication of internal shearing in the zone of soil on top of the plate and distributed shear bands developing especially towards the leading edge of the anchor. Also, the extent of soil mass that is moving with approximately the same displacement as the anchor (e.g. $\delta_{soil}/\delta > 0.9$) progressively decreases as the load inclination (θ) increases. For example, for a load inclination of θ = 45° and for a relative density of R_D = 70%, the height of soil above the plate where the displacement δ_{soil}/δ > 0.9 is 0.35*B* compared with a height of 3.5*B* when the loading is vertical (θ = 0°).

The numerical results for θ > 60° show a non-linear dependence of $N_{\gamma,H}/N_{\gamma,V(\theta=0°)}$ on θ (Fig. 10), which suggests a change in failure mechanism at a load inclination of around θ = 75°. This also manifests as a 'kink' in the simulated responses on Fig. 9, particularly evident for θ = 85° at δ/B = 4.8% (R_D = 30%) and δ/B = 7.2% (R_D = 70%). The corresponding mechanisms on Fig. 11 (i.e. for θ = 85°) deviate markedly from the inverted trapezoid mechanism (for θ < 60°) to a more localised mechanism with the plate movement essentially 'dragging' the soil mass immediately above and adjacent in the direction of loading. The zone of intense shearing for these cases is essentially concentrated just on top of the plate. The displacement contours show indications of additional lateral capacity developing as bearing resistance on the front edge of the plate becomes mobilised at the higher load inclinations.

Fig. 12(a) shows the mobilised stress ratio ($M = q/p'$) in the deviatoric plane for an element of soil above the anchor at θ = 75° and 85°, with *M* peaking at 1.26 and 1.36 for R_D = 30% and 70% respectively. *M* then softens to a critical state value of 1.19 at δ/B = 12%. This value of *M* corresponds to a Lode angle of 15°, which is approximately equal to that obtained using the expressions provided in Potts & Gens (1984) for a Lode angle for a plane strain problem at failure. This ability of the model to capture the appropriate evolution of *M* in the simulations of the influencing domain (Fig. 12(a)) and ultimate reduction in *M* to critical state allows the user to successfully capture the progressive failure mechanism, leading to realistic estimates of capacities; such a feature could not have been achieved within routinely used limit algorithms that analyse geotechnical problems on an impending state of failure.

It is also instructive to examine the true mobilised friction angle ($\sin\phi = (\sigma_1 - \sigma_3)/(\sigma_1 + \sigma_3)$) in the simulations, as shown by Fig. 12(b). The numerical simulations at R_D = 70% produce a maximum mobilised ϕ of 45.2° followed by softening to a critical state value of 36.6°, that is about 4.4° higher than ϕ_c in triaxial compression for the same sand. For the same sand, over stress levels between 10 kPa and 100 kPa and at a relative density, R_D = 80%, Lehane & Liu (2013) reported direct shear friction angles ($\phi_{ds} = \tan^{-1}(\tau_{xy}/\sigma_y)$) of ~ 40°.

Considering that ϕ_{ds} measured in direct shear can be 5° to 6° lower than the true mobilised friction angle (Pradhan et al. 1988, Lings & Dietz 2004), the simulations appear to produce justifiable results.

Comparison of the numerical and experimental results

The numerical simulations support the experimental evidence (presented earlier in the paper) that the anchor capacity factor for horizontal loading ($N_{\gamma,H(\theta=90°)}$) is higher than for vertical loading (($N_{\gamma,V(\theta=0°)}$), with the (numerically determined) ratio ranging between 1.5 and 1.65 (for H/B = 2) and between 1.22 and 1.58 (for H/B = 4) for different values of R_D. This decreasing trend with increasing H/B is somewhat reflected in the experiments, with the experimentally observed ratios varying in range of 1.9 to 2.02 (for H/B = 2) and ~1.75 (for H/B = 4). Since the plates used for the centrifuge experiments were relatively rough and failure is expected to occur in the influence zone around the plate and not at the anchor-sand interface, an attempt has been made to compare the experimental results (excluding the H/B = 3.83 results in loose sand as these reflect a slightly lower soil density, as noted earlier in the paper) with the numerical results in Fig. *13*. To facilitate the comparison, a shape factor (S_f) for a horizontal plate anchor has been used to reduce the experimental results to an equivalent plane strain anchor, that takes into account the transition from a possible 2-D wedge to a 3-D block in the influence zone due to a change in the geometry of the plate from strip to rectangular. Dickin (1988) showed that S_f was R_D and H/B dependent, and proposed that S_f be calculated as:

$$S_f = 1 - \frac{jB}{3LH}(6B - 7H) \qquad (27a)$$

where j is 1.0 for R_D = 76% and 0.4 for R_D = 33% in Erith sand. To account for the slightly different R_D values in the experiments reported here, j was calculated by linearly interpolating between the limits 0.4 and 1.0 for R_D = 33% and 76% respectively, as per the following expression:

$$j = 0.0132\, R_D(\%) - 0.013 \qquad (27b)$$

For average relative densities for the loose and dense sand states of R_D = 45% and 70%, Eqn. (27b) gives j = 0.6 and 0.92 respectively. The corresponding shape factors were calculated using Eqn. (27a), and applied to the experimental data in Fig. *13*. For these few simulations, K_0 was taken as 0.4 as per the original form of Jaky's expression as noted in Mesri & Hayat (1993) as this gave overall better agreement than the commonly adopted simplified version, $K_0 = 1 - \sin\phi_c \sim$ 0.5. The comparisons between the simulations and the experiments provided in Fig. 13, show satisfactory agreement, where it is evident that the trends observed in the experiments are also replicated by the numerical simulations, albeit that the agreement between the measurements and simulations is less convincing for the cases in loose sand at *H*/*B* = 2.83. Although adjustments to the adopted values for S_f or K_0 for the numerical simulations would lead to better agreement for particular cases, the motivation for the comparisons was to assess if the trends and dependencies observed in the numerical data are supported by experimental observations, which they are.

Interaction diagram for plate anchor capacity

Anchor resistance factors $N_{\gamma,V}$ and $N_{\gamma,H}$ corresponding to peak anchor capacity from each of the numerical probe analyses are represented as interaction diagrams in Fig. 14. The size of the interaction diagrams depends on *H/B*. For example, the peak values of $N_{\gamma,V}$ and $N_{\gamma,H}$ increase by a factor of ~1.5 and ~2 as *H/B* increases from 2 to 4 respectively. For a given R_D and *H/B*, there is little interaction between $N_{\gamma,V}$ and $N_{\gamma,H}$ for $\theta < 60°$, i.e. $N_{\gamma,V}$ remains approximately constant up to $\theta = 60°$. At $\theta > 60°$, $N_{\gamma,V}$ reduces with increasing $N_{\gamma,H}$, with the interaction diagram approaching the $N_{\gamma,H}$ axis at a value that depends on both *H*/*B* and R_D. An interesting and important observation from Fig. 14 is that the approach to the $N_{\gamma,H}$ axis has a negative gradient – as also observed in the experimental data on Fig. 7 – which suggests that the maximum $N_{\gamma,H}$ would be obtained at a negative value of $N_{\gamma,V}$, i.e. at $\theta > 90°$.

This uncertainty in the maximum $N_{\gamma,H}$ causes an associated uncertainty in the shape of the interaction diagram. In an attempt to resolve this, a number of 'swipe' analyses were conducted at *H/B* = 3 and 4 for R_D = 70%. A swipe analysis involves a displacement controlled probe at a given direction (θ in Fig. 15) to an initial state of collapse, followed by either pure horizontal displacement with no change in vertical displacement (i.e. a 'forward swipe'; black markers in Fig. 15), or pure vertical displacement with no change in horizontal displacement (i.e. a 'reverse swipe'; red markers in Fig. 15). The results of these analyses are shown in Fig. 15 together with a further displacement-controlled probe analysis at $\theta = 95°$ (i.e. the plate displaced with a small downward component as it is sheared horizontally). Both axes on Fig. 15 are normalised by the pure anchor resistance factor for vertical loading (i.e. $N_{\gamma,V(\theta=0°)}$), such that the swipes approach the vertical axis at $N_{\gamma,V}/N_{\gamma,V(\theta=0°)}$ ~1, and the horizontal axis at $N_{\gamma,H}/N_{\gamma,V(\theta=0°)}$ ~1.5, with $N_{\gamma,H}/N_{\gamma,V(\theta=0°)}$ increasing further as $N_{\gamma,V}/N_{\gamma,V(\theta=0°)}$ becomes progressively more negative.

As the shape of interaction diagrams for buried objects in sand remains a relatively unexplored domain in geomechanics, insights available from existing studies on interaction diagram of a surface footing (i.e. at *H/B* = 0 as shown by Case A in Fig. 16) in sand (e.g. Loukidis et al. 2008, Gottardi & Butterfield 1993) have been used here to describe the interaction diagram algebraically. Fig. 16 provides potential interaction diagram shapes for different levels of footing (or plate) embedment, with positive and negative values of $N_{\gamma,V(\theta=0°)}$ representing tensile and compressive capacity respectively. The shape abc in Fig. 16 is typical of the well-established interaction diagram for a surface footing (case A), intersecting the vertical axis at $N_{\gamma,V(\theta=0°)}$ (for drained tensile loading), and with a maximum $N_{\gamma,H}$ occurring at around $0.45N_{\gamma,V(\theta=180°)}$ (Loukidis et al. 2008, Bienen et al. 2007). As the plate becomes embedded, qualitative assessment of the problem indicates that the interaction diagram is expected to grow to a′b′c′, a″b″c″, etc., with (a) a gradually increasing $N_{\gamma,V(\theta=0°)}$ due to overburden pressure and the uplift kinematics at increasing embedment; (b) an increasing $N_{\gamma,V(\theta=180°)}$ component due to the added effect of surcharge, and (c) possible upward shift of the point of maximum $N_{\gamma,H}$ (b, b′, b″) as deep failure conditions are approached. A single displacement probe at θ = 95° (although not reaching peak capacity due to numerical instabilities) was undertaken for *H/B* = 3 and 4 with R_D = 70% (Fig. 15) and shows that $N_{\gamma,H}$ in the footing domain (θ > 90°) is indeed higher than $N_{\gamma,H}$ for θ < 90° (anchor domain). Although rigour would require that the entire interaction diagram is described acceptably, a more pragmatic approach is adopted here, whereby the interaction diagram is fitted for 0° < θ < 90° (i.e. a′ b′ in Fig. 16), justified by the scope of the problem of interest and also by the lack of data, and hence confidence, for θ > 90°.

The numerical interaction diagrams are described algebraically in Fig. 17 by:

$$\left(\frac{N_{\gamma,H}}{a_1\, N_{\gamma,V(\theta=0°)}}\right)^{a_2} + \left(\frac{N_{\gamma,V}}{N_{\gamma,V(\theta=0°)}}\right)^{a_3} = 1 \qquad (28)$$

where a_1 controls the intercept on the $N_{\gamma,H}$ axis and a_2 and a_3 control the shape close to the $N_{\gamma,V}$ axis and $N_{\gamma,H}$ axis respectively. Best fits to the numerical data using Eqn. (28) are represented by the dashed lines in Fig. 17, with values of the constants a_1, a_2 and a_3 summarised in Table 6. It is observed that a_1 and a_2 are *H/B* and R_D dependent, whereas a_3 = 1.05 works well for all cases.

The increase in a_1 with R_D reflects a higher mobilised ϕ for dense soils over loose soils, resulting in a higher $N_{\gamma,H}$ with respect to $N_{\gamma,V}$. The value of a_2 decreases with increasing R_D, resulting in a sharper change in $N_{\gamma,V}$ close to the maximum $N_{\gamma,V}$ axis as the sand gets denser. Both a_1 and a_2 decrease with increasing *H*/*B*, resulting in a progressive inward shift of the interaction diagram as the plate becomes deeper. This could be attributed to changing stress levels; however, this would require confirmations through further analyses at deeper plate embedments. Finally, the approximately linear dependence of $N_{\gamma,H}$ with $N_{\gamma,V}$ close to the horizontal axis (for a_3 close to 1) is consistent with parabolic interaction diagram for surface footings (i.e. for *H*/*B* = 0 and θ ranging between 90° and 180°) (Loukidis et al. 2008, Govoni et al. 2011). In the absence of further numerical and centrifuge data at deeper embedments, it may be reasonable to use the current interaction diagram at shallow embedment ratios across different stress and density levels if:

- the ratio of $N_{\gamma,H}/N_{\gamma,V(\theta=0°)}$ is first determined from Fig 10,
- a stress or R_D dependent $N_{\gamma,V(\theta=\,0°)}$ is determined (e.g. using the semi-empirical approaches outlined in White et al. 2008), and
- the constants a_1, a_2 and a_3 are interpolated as per the required *H*/*B* or R_D from Table 6.

Conclusions

This study explores the effect of load inclination on horizontal plate anchors in sand through a combination of centrifuge and FE modelling. The experimental data show the expected increase in anchor capacity with increasing relative density and embedment depth for vertical loading, and also an increase in anchor capacity as the load inclination becomes more horizontal, with anchor capacity under pure horizontal loading being approximately 1.7 times than that under pure uplift. Such an increase would be incompatible with frictional capacity mobilisation at the anchor-sand interfaces and passive bearing resistance at the anchor edge. Finite element analyses using a bounding surface plasticity model support the experimental measurements, with the mechanism for pure vertical uplift at shallow embedment resembling the well-established inverted trapezoid with a tendency for the slip planes to curve outwards at shallow embedment due to higher dilatancy at lower stress levels. As the load inclination becomes progressively more horizontal, the mechanism skews towards the direction of loading, involving a zone of soil above and adjacent to the plate even when the loading is purely horizontal.

A detailed numerical parametric study that takes account of the effects of relative density, stress level and loading and fabric anisotropy in mobilised friction and dilation, yielded results that were qualitatively consistent with the trends obtained from the experiments. Vertical component of anchor capacity is generally unaffected at load inclinations up to 60°, while the horizontal component increases steadily. This is due to longer (inclined) slip planes and passive resistance from a larger influence zone, along with the associated changes in direction of major principal stresses in the influence zone above the plate. At load inclinations greater than 60°, the decrease in the vertical component of anchor capacity is outweighed by the increase in the horizontal component of capacity, such that the net anchor capacity is higher. When the loading direction is near horizontal, the mechanism still involves a zone of soil above and adjacent to the plate along with lateral bearing resistance developing along the leading edge of the plate.

The numerical results allowed an interaction diagram for peak plate anchor capacity to be formulated, the shape of which is a function of relative density and embedment ratio. These simple interaction diagram equations allow the plate anchor capacity to be calculated under an inclined load at shallow embedment. However, further investigation is required to understand the potential transformation of the shape of the interaction diagram as the plate moves deeper and into the footing domain.

Acknowledgements

This work forms part of the activities of the Centre for Offshore Foundation Systems (COFS), currently supported as a Centre of Excellence by the Lloyd's Register Foundation. The Lloyd’s Register Foundation invests in science, engineering and technology for public benefit, worldwide. The first author would also like to acknowledge the contribution of Andrea Diambra from University of Bristol for the initial idea and motivation for this research.

References

Bhattacharya, P. & Kumar, J., 2014. Geomechanics and Geoengineering : An International Vertical pullout capacity of horizontal anchor plates in the presence of seismic and seepage forces. *Geomechanics and Geoengineering: An International Journal*, 9(4), pp.294–302.

Bienen, B., Gaudin, C. & Cassidy, M.J., 2007. Centrifuge tests of shallow footing behaviour on sand under combined vertical-torsional loading. *International Journal of Physical Modelling in Geotechnics*, 7(2), pp.01-21.

Bolton, M.D., 1986. The strength and dilatancy of sands. *Géotechnique*, 36(1), pp.65–78.

Cheuk, C.Y., White, D.J. & Bolton, M.D., 2008. Uplift Mechanisms of Pipes Buried in Sand. *Journal of Geotechnical and Geoenvironmental Engineering*, 134(2), pp.154–163.

Choudhary, A.K. & Dash, S.K., 2013. Uplift Behaviour of Horizontal Plate Anchors Embedded in Geocell-Reinforced Sand. , pp.3–7.

Chow, S.H., O'Loughlin, C.D., Gaudin, C. & Lieng, J.T , 2018a. Drained monotonic and cyclic capacity of a dynamically installed plate anchor in sand. *Ocean Engineering*, 148(September 2017), pp.588–601.

Chow, S.H., Le, J., Forsyth, M. & O'Loughlin, C.D., 2018b. Capacity of vertical and horizontal plate anchors in sand under normal and shear loading. In *International Conference on Physical Modelling in Geotechnics*. pp. 559–564.

Chow, S.H., Bienen, B. & Randolph, M.F., 2018c. Rapid penetration of piezocones in sand. In *Cone Penetration Testing 2018*. pp. 213–219.

Chow, S.H., Roy, A., Herduin, M., Heins, E., King, L. Bienen, B., O'Loughlin, C.D., Gaudin, C. & Cassidy, M.J., 2019. *Characterisation of UWA superfine silica sand. Ocean Graduate School Technical report, The University of Western Australia, GEO 18844*,

Dafalias, Y.F. & Manzari, M.T., 2004. Simple Plasticity Sand Model Accounting for Fabric Change Effects. *Journal of Engineering Mechanics*, 130(6), pp.622–634.

Dafalias, Y.F., Papadimitriou, A.G. & Li, X.S., 2004. Sand plasticity model accounting for inherent fabric anisotropy. *Journal of Engineering Mechanics*, 130(11), pp.1319–1333.

Dickin, E.A., 1988. Uplift behavior of horizontal anchor plates in sand. *Journal of geotechnical engineering*, 114(11), pp.1300–1317.

Dove, J.E. & Jarrett, J.B., 2002. Behavior of Dilative Sand Interfaces in a Geotribology Framework. *Journal of Geotechnical and Geoenvironmental Engineering*, 128(1), pp.25–37.

Fontana, C.M., Arwade, S.R., DeGroot, D.J., Myers, A.T., Landon, M. & Aubeny, C, 2016. Efficient multiline anchor systems for floating offshore wind turbines. In *35th International Conference on Ocean, Offshore and Arctic Engineering*.

Gaudin, C., O'Loughlin, C.D., Duong, M.T., Herduin, M., Fiumana, N., Draper, S., Wolgamot, H., Zhao, L. & Cassidy, M.J., 2017. New anchoring paradigms for floating renewables. *European Wave and Tidal Energy Conference*.

Gottardi, G. & Butterfield, R., 1993. On the bearing capacity of surface footings on sand under general planer loads. *Soils and Foundations*, 33(3), pp.68–79.

Govoni, L., Gourvenec, S. & Gottardi, G., 2011. A centrifuge study on the effect of embedment on the drained response of shallow foundations under combined loading. *Géotechnique*, 61(12), pp.1055–1068.

Hallowell, S.T., Arwade, S.R., Fontana, C.M., DeGroot, D.J., Aubeny, C., Diaz, B.D., Myers, A.T. & Landon, M., 2018. System reliability of floating offshore wind farms with multiline anchors. *Ocean Engineering*, 160(February), pp.94–104.

Han, C., 2016. Performance of plate anchors under sustained loading. PhD thesis, The University of Western Australia.

Hao, D., Fu, S. & Rong, C., 2014. Numerical Analysis of Uplift Capacity of Circular Plate Anchor in Sand. *Journal of geotechnical engineering*, 19, pp.18947–18961.

Kumar, J. & Sahoo, J.P., 2012. Upper Bound Solution for Pullout Capacity of Vertical Anchors in Sand Using Finite Elements and Limit Analysis. *International Journal of Geomechanics*, 12(3), pp.333–337.

Lehane, B.M. & Liu, Q.B., 2013. Measurement of Shearing Characteristics of Granular Materials at Low Stress Levels in a Shear Box. *Geotechnical and Geological Engineering*, 31(1), pp.329–336.

Li, X.S. & Dafalias, Y.F., 2012. Anisotropic Critical State Theory: Role of Fabric. *Journal of Engineering Mechanics*, 138(3), pp.263–275.

Li, X.S. & Wang, Y., 1998. Linear Representation of Steady-State Line for Sand. *Journal of Geotechnical and Geoenvironmental Engineering*, 124(12), pp.1215–1217.

Lings, M.L. & Dietz, M.S., 2004. An improved direct shear apparatus for sand. *Géotechnique*, 54(4), pp.245–256.

Liu, J.Y., Liu, M.L. & Zhu, Z.D., 2012. Sand Deformation around an Uplift Plate Anchor. *Journal of Geotechnical and Geoenvironmental Engineering*, 138(6), pp.728–737.

Loukidis, D., 2006. *Advanced Constitutive Modeling of Sands and Applications to foundation Engineering*. Purdue University.

Loukidis, D., Chakraborty, T. & Salgado, R., 2008. Bearing capacity of strip footings on purely frictional soil under eccentric and inclined loads. *Canadian Geotechnical Journal*, 45(6), pp.768–787.

Loukidis, D. & Salgado, R., 2011. Effect of relative density and stress level on the bearing capacity of footings on sand. *Géotechnique*, 61(2), pp.107–119.

Loukidis, D. & Salgado, R., 2009. Modeling sand response using two-surface plasticity. *Computers and*

Geotechnics, 36(1–2), pp.166–186.

Merifield, R.S. & Sloan, S.W., 2006. The ultimate pullout capacity of anchors in frictional soils. *Canadian Geotechnical Journal*, 43(8), pp.852–868.

Mesri, G. & Hayat, T.M., 1993. The coefficient of earth pressure at rest: Discussion. *Canadian Geotechnical Journal*, 30(5), pp.647–666.

O'Neill, M.P., Bransby, M.F. & Randolph, M.F., 2003. Drag anchor fluke-soil interaction in clays. *Canadian Geotechnical Journal*, 40(1), pp.78–94.

Paikowsky, S.G., Player, C.M. & Connors, P.J., 1995. A dual interface appaartus for testing unrestricted friction of a soil along solid surfacs. *Geotechnical Testing Journal*, 18(2), pp.168–193.

Papadimitriou, A.G., Dafalias, Y.F. & Yoshimine, M., 2005. Plasticity modelling of the effect of sample preparation method on sand response. *Soils and Foundations*, 45(2), pp.109–123.

Petalas, A.L., Dafalias, Y.F. & Papadimitriou, A.G., 2019. SANISAND-FN: An evolving fabric-based sand model accounting for stress principal axes rotation. *International Journal for Numerical and Analytical Methods in Geomechanics*, 43(1), pp.97–123.

Potts, D.M. & Gens, A., 1984. the Effect of the Plastic Potential in Boundary Value Problems Involving Plane Strain Deformation. *International Journal for Numerical & Analytical Methods in Geomechanics*, 8(259–286).

Pradhan, T.B.S., Tatsuaka, F. & Horii, N., 1988. Strength and deformation characteristics of sand in torsional simple shear. *Soils and Foundations*, 28(3), pp.131–148.

Roy, A., Chow, S.H. , O'Loughlin, C.D., Randolph, M.F., 2019. Effect of stress history and shallow embedment on centrifuge cone penetration tests in sands, *Proceedings of the 38th International Conference on Offshore Mechanics and Arctic Engineering, Glasgow*

Roy, A., Chow, S.H., O'Loughlin, C.D.,Randolph, M.F. & Whyte, S., 2020. Use of a bounding surface model in predicting element tests and capacity in simple boundary value problems. *Canadian Geotechnical Journal*, doi.org/10.1139/cgj-2019-0841

Sakai, T. & Tanaka, T., 2007. Experimental and Numerical Study of Uplift Behavior of Shallow Circular Anchor in Two-Layered Sand. *Journal of Geotechnical and Geoenvironmental Engineering*, 133(4), pp.469–477.

Sheng, D., Sloan, S.W. & Yu, H.S., 2000. Aspects of finite element implementation of critical state models. *Computational Mechanics*, 26(2), pp.185–196.

Smith, C.C., 2012. Limit loads for a shallow anchor/trapdoor embedded in a non-associative Coulomb soil. *Géotechnique*, 62(7), pp.563–571.

Uesugi, M. & Kishida, H., 1986. Frictional resistance at yield between dry sand and mild steel. *Soils and Foundations*, 26(4), pp.139–149.

White, D.J., Cheuk, C.Y. & Bolton, M.D., 2008. The uplift resistance of pipes and plate anchors buried in sand. *Géotechnique*, 58(10), pp.771–779.

Yamamoto, N., 2006. *Numerical analysis of shallow circular foundations on sands*. PhD thesis, The University of Western Australia.

Yang, M., Murff, J.D. & Aubeny, C.P., 2010. Undrained capacity of plate anchors under general loading. *Journal of Geotechnical and Geoenvironmental Engineering*, 136(10), pp.1383–1393. .

Table Captions

Table 1: Physical properties of UWA Silica sand

Table 2: Centrifuge test program and result summary (N = 20g)

Table 3: Parameters with the governing equations and calibration technique

Table 4 : Model parameters for UWA silica sand

Table 5 : Mesh sensitivity study details

Table 6 : Constants used in Eqn. (28) to describe the interaction diagram

Figure captions

Fig. 1: Plate anchor orientation and loading: (a) vertical orientation under horizontal loading, (b) horizontal orientation under vertical loading, (c) inclined orientation under inclined loading, (d) horizontal orientation under inclined loading

Fig. 2 : Centrifuge model plate anchor details for: (a) θ = 0°, (b) θ = 30° and 60°, (c) θ = 90° (d) connection details for bridle

Fig. 3 : Centrifuge test setup details for (a) θ = 0° (b) θ = 30°, 60° (c) θ = 90°

Fig. 4 : Placement of plate anchors in centrifuge strongbox during preparation

Fig. 5 : Measured cone tip resistance profiles and recomputed R_D before and after anchor tests in: (a) dense sand samples (b) loose sand samples

Fig. 6 : Normalised anchor capacity responses for: (a) H/B = 1.83 in dense sand, (b) H/B = 1.83 in loose sand, (c) H/B = 2.83 in dense sand, (d) H/B = 2.83 in loose sand, (e) H/B = 3.83 in dense sand, (f) H/B = 3.83 in loose sand

Fig. 7 : Interaction diagram of plate anchors at different embedment ratios in: (a) loose sand, (b) dense sand

Fig. 8: Typical mesh details and boundary conditions for the anchor problem in Abaqus (H/B = 4)

Fig. 9: Vertical and horizontal anchor resistance factors at different load inclinations at H/B = 4: (a) horizontal resistance in dense sand (R_D = 70%), (b) vertical resistance in dense sand (R_D = 70%), (c) horizontal resistance in loose sand (R_D = 30%), (d) vertical resistance in loose sand (R_D =30%)

Fig. 10: Variation of peak normalised horizontal anchor factor with load inclination

Fig. 11 : Numerically determined failure mechanisms at H/B = 4 compared against displacement contours (shown by red dashed lines)

Fig. 12: (a) Variation of (a) mobilised stress ratio M (= q/p') and (b) mobilised friction angle, ϕ for an element above the plate at an embedment ratio, H/B = 4 loaded at θ = 75° and 85° in loose and dense sand

Fig. 13: Comparison of measured and simulated anchor capacity for different load inclinations and embedment ratios in: (a) dense sand (R_D = 70%) (b) loose sand (R_D = 40%)

Fig. 14: Interaction diagrams for peak plate anchor capacity at: (a) *H*/*B* = 2, (b) *H*/*B* = 3, (c) *H*/*B* = 4

Fig. 15: Extended interaction diagrams from swipe analyses in dense sand at: (a) *H*/*B* = 3 (b) *H*/*B* = 4

Fig. 16: Potential interaction diagrams for surface and embedded footings in sand

Fig. 17: Interaction diagrams for plate capacity at (a) *H*/*B* = 2, (b) *H*/*B* = 3, (c) *H*/*B* = 4

Table 1: Physical properties of UWA Silica sand (Chow et al. 2019)

Soil properties	**UWA Silica sand**
Angularity	Sub-rounded to sub-angular
Maximum void ratio (e_{max})[a]	0.789
Minimum void ratio (e_{min})[a]	0.512
Specific gravity[b]	2.67
Uniformity Coefficient (U)	1.73
Particle mean size (d_{50})	0.2 mm

[a] Maximum and minimum void ratios calculated as per AS 1289.5.5.1
[b] Maximum and minimum void ratios calculated as per AS 1289.3.5.1

Table 2: Centrifuge test program and result summary (N = 20g)

Box ID	**Average R_D, (%)**	**Unit weight, γ' (kN/m^3)**	**θ (°)**	**H/B**	**Measured load, F_m (N)**	**Corrected load (for anchor weight and/or line friction), F_c (N)**	**$N_\gamma = \frac{F_c}{AH\gamma}$**
2_L	47.35	15.8	0	1.83	82.9	63.7	2.08
			30	1.83	86.4	74.0	2.42
			60	1.83	112.9	105.7	3.46
			90	1.83	139.6	121.3	3.96
3_L	47.37	15.79	0	2.83	174.6	155.4	3.32
			30	2.83	184.4	171.9	3.67
			60	2.83	262.1	255.0	5.45
			90	2.83	306.4	278.8	5.96
4_L	44.74	15.72	0	3.83	221.1	201.8	3.24
			30	3.83	248.9	236.5	3.79
			60	3.83	274.5	267.3	4.28*
			90	3.83	584.1	357.2	5.72
2_D	69.53	16.41	0	1.83	110.0	90.7	2.85
			30	1.83	134.8	122.3	3.85
			60	1.83	156.1	148.9	4.69
			90	1.83	211.9	183.3	5.77
3_D	71.3	16.45	0	2.83	231.2	211.9	4.35
			30	2.83	257.0	244.5	5.01
			60	2.83	322.8	315.6	6.48
			90	2.83	401.2	357.7	7.34
4_D	74.3	16.54	0	3.83	436.9	417.7	6.36
			30	3.83	499.4	486.8	7.41
			60	3.83	502.6	495.2	7.54
			90	3.83	662.2	598.0	9.1*

* Bridle on anchor / mooring line failed.

Table 3: Model governing parameters and equations

Parameters	Description	Governing equations (Eqn. No)	Notes/Reference
e_o	Controls the intercept of the CSL at very low mean stress levels in e- $(p'/P_a)^{\xi}$ space	$e_c = e_o - \lambda_c \left(p'/P_a\right)^{\xi}$ (1) $\psi = (e - e_c)$ (2)	Li & Wang (1998), Dafalias & Manzari (2004)
λ_c	Controls the slope of the CSL in e- $(p'/P_a)^{\xi}$ space		
ξ	Influences the linearisation of the CSL with p'		
M	Controls the critical state stress ratios in triaxial compression		
c_1	Controls the critical state stress ratios in triaxial extension		
G_0	Elastic shear modulus	$G = G_0 P_a \frac{(2.97-e)^2}{(1+e)} \left(\frac{p'}{P_a}\right)^{1/2}$ (3) $K = G\, \frac{2(1+\nu)}{3(1-2\nu)}$ (4) $d\varepsilon_e^e = ds/2G$ (5) $d\varepsilon_v^e = dp/K$ (6)	Dafalias & Manzari (2004)
ν	Poisson's ratio		
m	Controls the size of the yield surface	$f = [(\mathbf{r}-\boldsymbol{\alpha}):(\mathbf{r}-\boldsymbol{\alpha})\,]^{1/2} - \sqrt{2/3}\, m = 0$ (7)	Dafalias & Manzari (2004)
n^d, n^b	Influences the mobilised stress ratio at peak friction angle and at phase transformation	$\boldsymbol{\alpha}_{\boldsymbol{\theta}}^{\mathbf{a}} = \sqrt{\frac{2}{3}}(M_\theta^a - m)n$ ($a = b, d, c$) (8) $M_\theta^c = g_1(\theta_l, c_1)M$ (9) $g_1(\theta_l, c_1) = \left(\frac{2{c_1}^4}{((1+c_1^4)-(1-c_1^4)\cos 3\theta_l)}\right)^{1/4}$ (10) $M_\theta^b = \left[M_\theta^c \exp\left(-n^b\, \psi_f\right)\right]$ (11)* $M_\theta^d = \left[M_\theta^c \exp\left(n^d \psi_f\right)\right]$ (12)*	Dafalias & Manzari (2004), Sheng et al. (2000)
c_h , h_{in}	Plastic modulus constants	$K_p = \frac{2}{3} p'\, h\left(\boldsymbol{\alpha}_{\boldsymbol{\theta}}^{\mathbf{b}} - \boldsymbol{\alpha}\right):\mathbf{n}$ (13) $h = \frac{b_o}{(\boldsymbol{\alpha}-\boldsymbol{\alpha}_{\mathbf{in}}):\mathbf{n}}$ (14) $b_o = h_0 G_0 (1 - c_h e)\left(\frac{p'}{P_a}\right)^{-1/2}$ (15) $h_0 = h_{in}\, f_h$ (16)*	Dafalias et al.(2004)
A_0	Parameter affecting the rate of dilatancy	$d\varepsilon^p = \langle L \rangle \mathbf{R}$ (17) $\frac{dg}{d\sigma} = \mathbf{R} = \mathbf{R}' + \frac{1}{3}D\mathrm{I} = B\mathbf{n} - C\left(\mathbf{n}^2 - \frac{1}{3}\mathrm{I}\right) + \frac{1}{3}D\mathrm{I}$ (18) $B = 1 + \frac{3(1-c_2)}{2c_2} g_2(\theta_l, c_2)\cos 3\theta_l,$	Dafalias et al.(2004), Loukidis & Salgado (2009)

c_2	Parameter affecting the slope of the plastic potential	$C = 3\sqrt{\frac{3}{2}}\frac{(1-\ c_2)}{c_2}g_2(\theta_l, c_2)$ $g_2(\theta_l, c_2) = \frac{2c_2}{(1+c_2)-(1-c_2)\cos 3\theta_l}$ (19) $D = A_0(\ \boldsymbol{\alpha}_{\boldsymbol{\theta}}^{\mathbf{d}} - \boldsymbol{\alpha}):\mathbf{n}$ (20)	
a	Parameter controlling the initial fabric	$F_{11} = 0.5(1-a)\ \ F_{22} = 0.5(1-a)\ \ F_{33} = a$ (21) $F_{ij} = 0\ \ (when\ i \neq j)$ $A = g_1(\theta_l, c_1)\ \mathbf{F}:\mathbf{n}$, (22) $A_c = -\ \left(\frac{1}{c_1}\right)A_e = \sqrt{\frac{3}{2}}\left(a - \frac{1}{3}\right)$ $A_{ratio} = 2 * \frac{A_e - A}{A_e - A_c}$ (23)	Dafalias et al.(2004)
b_1,b_2, k	Factors to scale the state parameter and plastic modulus for loading conditions other than triaxial compression	$f = \frac{1}{b_1 + b_2(A_{ratio})^{b_3}}$ (24)* $b_3 = \frac{\log(\frac{1-b_1}{b_2})}{\log 2}$ $f_h = \ f^k$ (25)* $\psi_f = f\psi$ (26)*	

Table 4 : Model parameters for UWA silica sand

Sanisand model parameters	Symbol	UWA silica sand
Elastic properties	G_0	135
	v	0.14*
Critical state properties	e_o	0.812
	λ	0.0189
	ξ	0.7
	M	1.296
	c_1	0.7*
Yield surface	m	0.05
Parameter for plastic potential gradient	c_2	0.78*
Parameters influencing plastic modulus	h_0	7.5
	c_h	1.01
	n^b	2
Parameters influencing dilatancy	A_0	0.84
	n^d	3.4
Anisotropy and state parameter scaling parameters	a	0.27
	b_1	2.5
	b_2	-0.833*
	k	1.5

*Assumed

Table 5 : Mesh sensitivity study details

Analysed cases	**Load inclination, θ (°)**	**Total elements in domain**	**Soil elements on plate (bias ratio)**	**Minimum size/thickness of element in soil**	**Anchor factor, N_γ**
H/B = 4, R_D = 70%	0	4223	20(2)	0.037B	3.33
		5257	30(2)	0.028B	3.27
		5557	35(2)	0.025B	3.23
		5915	37(2)	0.024B	3.23
H/B = 4, R_D = 30%	0	4223	20(2)	0.037B	2.94
		5257	30(2)	0.028B	2.9
		5557	35(2)	0.025B	2.94
		5915	37(2)	0.024B	2.91
H/B = 4, R_D = 70%	85	3213	12(2)	0.056B	5.49
		4027	20(2)	0.037B	5.19
		5994	31(2)	0.031B	4.8
		7570	34(2)	0.025B	4.69
		7701	40(2)	0.02B	4.72
H/B = 4, R_D = 30%	85	3213	12(2)	0.056B	3.86
		4027	20(2)	0.037B	3.7
		6024	31(2)	0.028B	3.46
		6908	30(2)	0.023B	3.47

Table 6 : Constants used in Eqn. (28) to describe the interaction diagram

R_D (%)	**H/B**	a_1	a_2	a_3
30	2	1.5	4.9	1.05
50	2	1.6	4.7	1.05
70	2	1.65	4.3	1.05
30	3	1.45	4.8	1.05
50	3	1.56	4.2	1.05
70	3	1.64	4.04	1.05
30	4	1.22	4.65	1.05
50	4	1.44	3.4	1.05
70	4	1.58	3.13	1.05

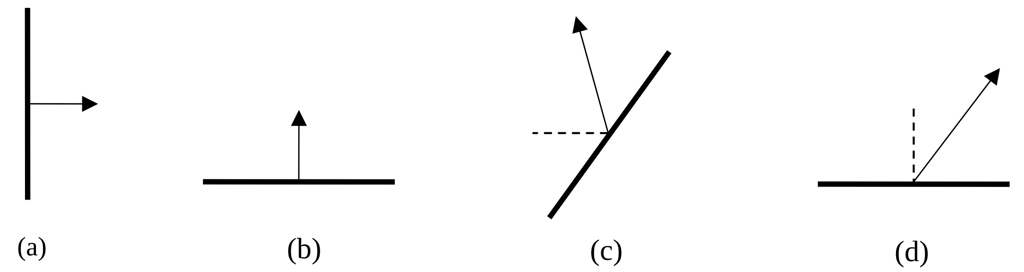

Fig. 1: Plate anchor orientation and loading: (a) vertical orientation under horizontal loading, (b) horizontal orientation under vertical loading, (c) inclined orientation under inclined loading, (d) horizontal orientation under inclined loading

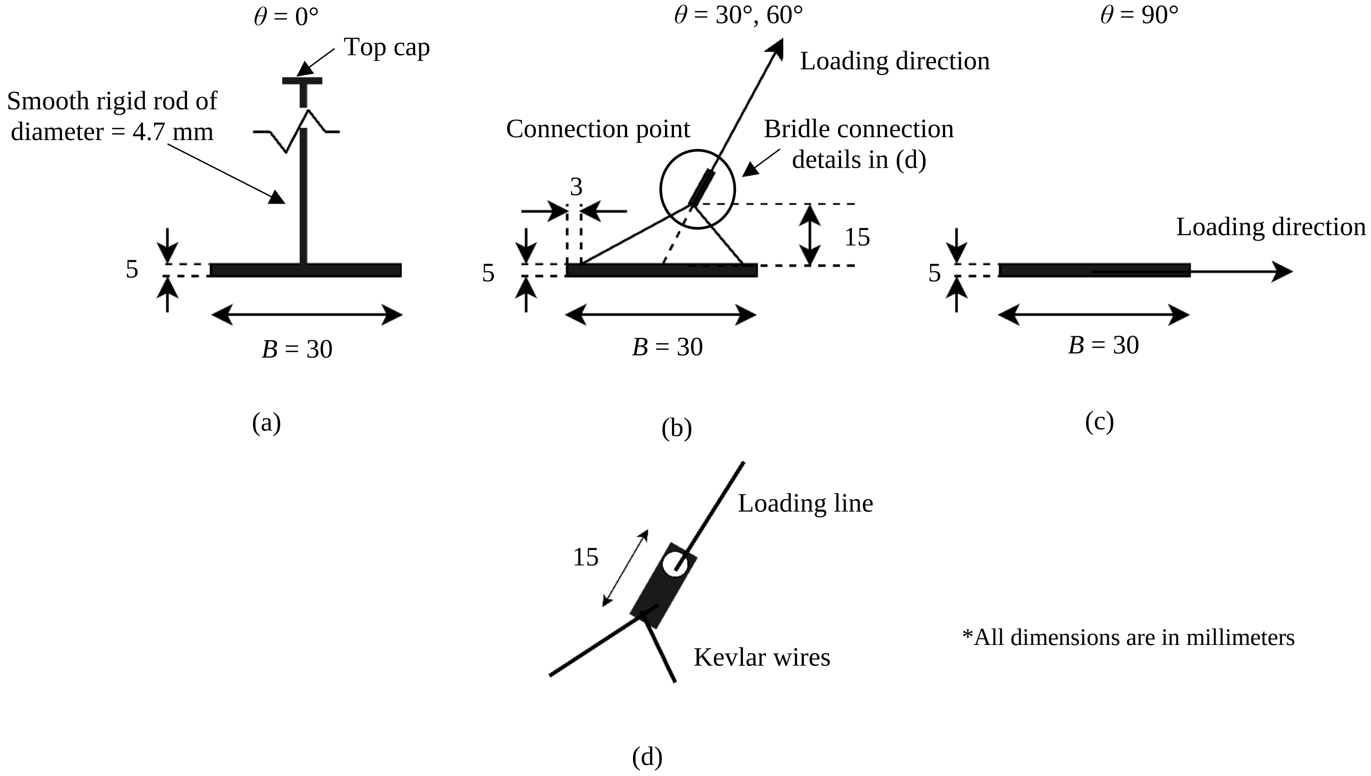

Fig. 2 : Centrifuge model plate anchor details for: (a) $\theta = 0°$, (b) $\theta = 30°$ and $60°$, (c) $\theta = 90°$ (d) connection details for bridle

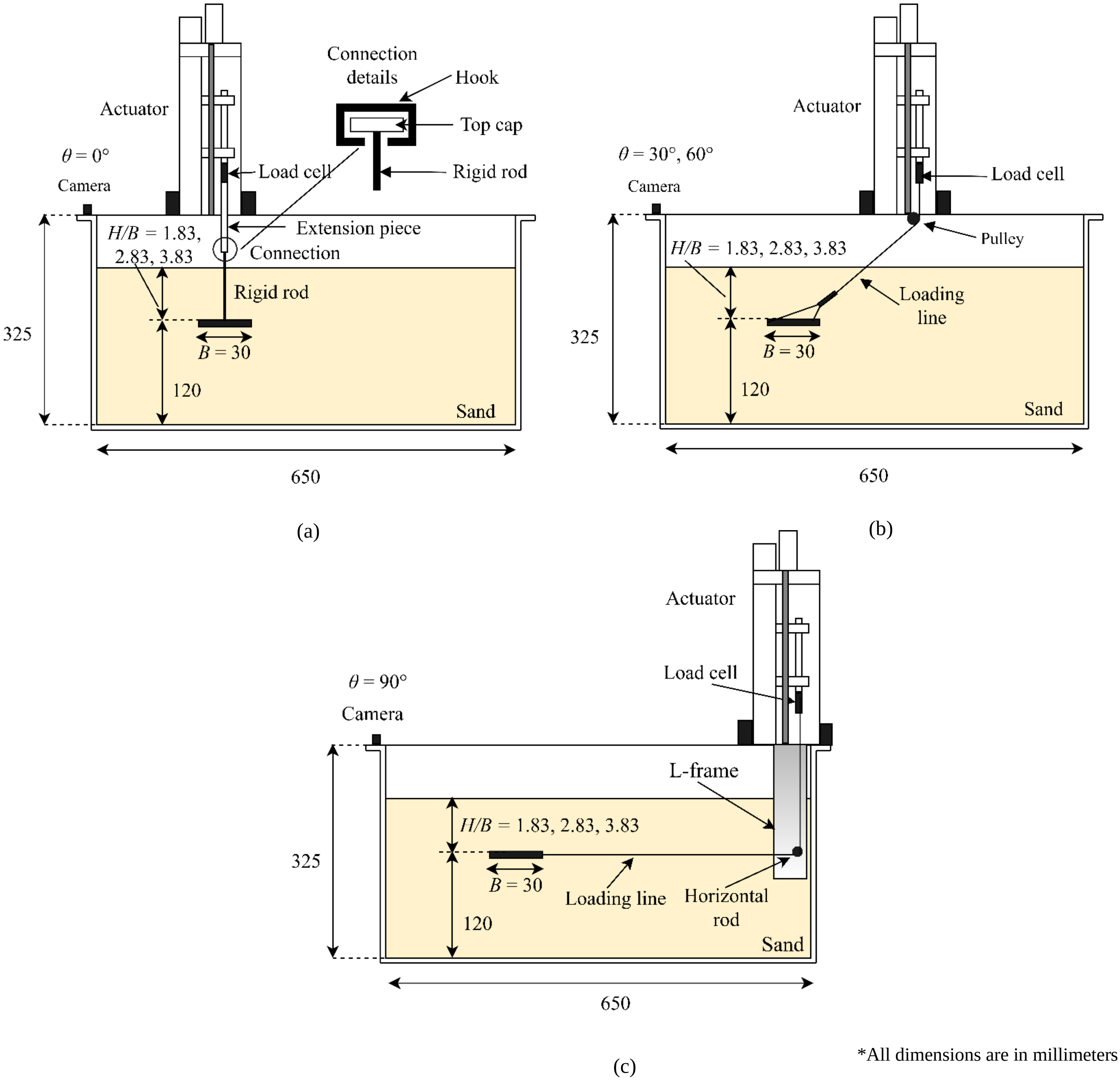

Fig. 3 : Centrifuge test setup details for (a) $\theta = 0°$ (b) $\theta = 30°, 60°$ (c) $\theta = 90°$

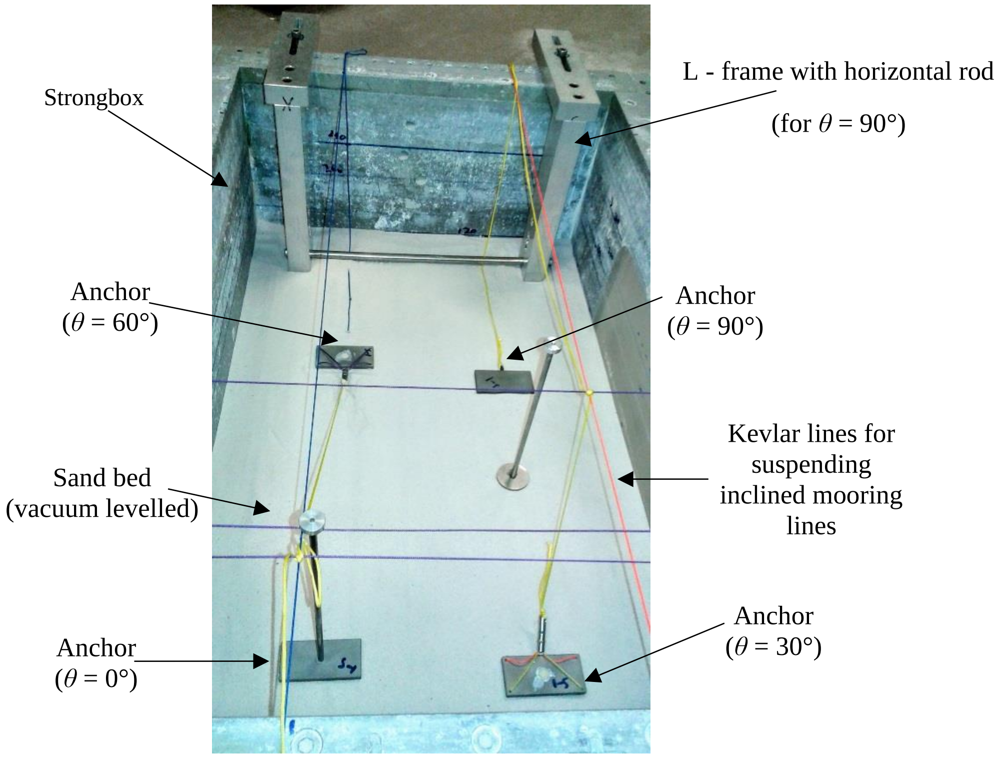

Fig. 4 : Placement of plate anchors in centrifuge strongbox during preparation

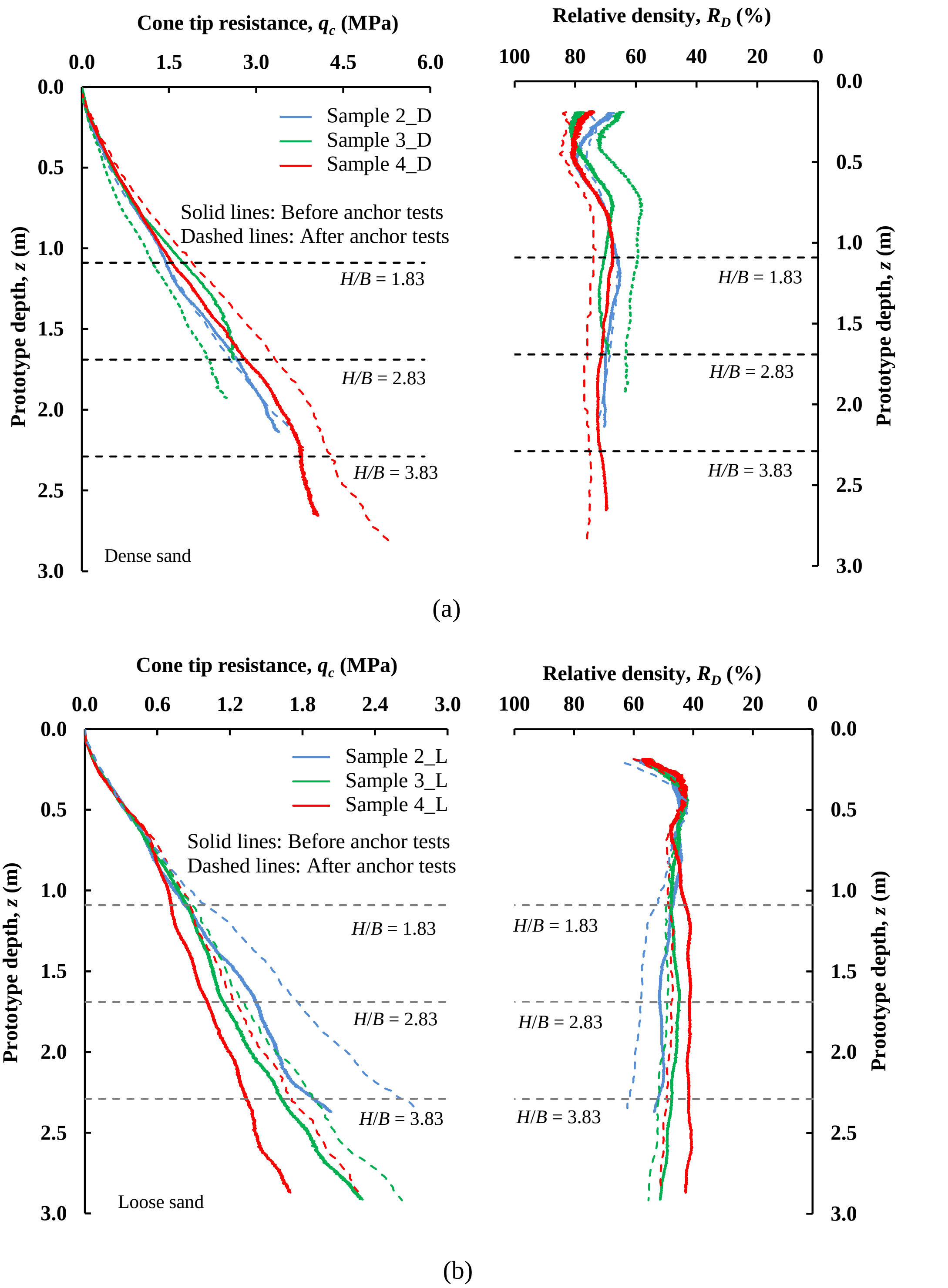

Fig. 5 : Measured cone tip resistance profiles and recomputed R_D before and after anchor tests in: (a) dense sand samples (b) loose sand samples

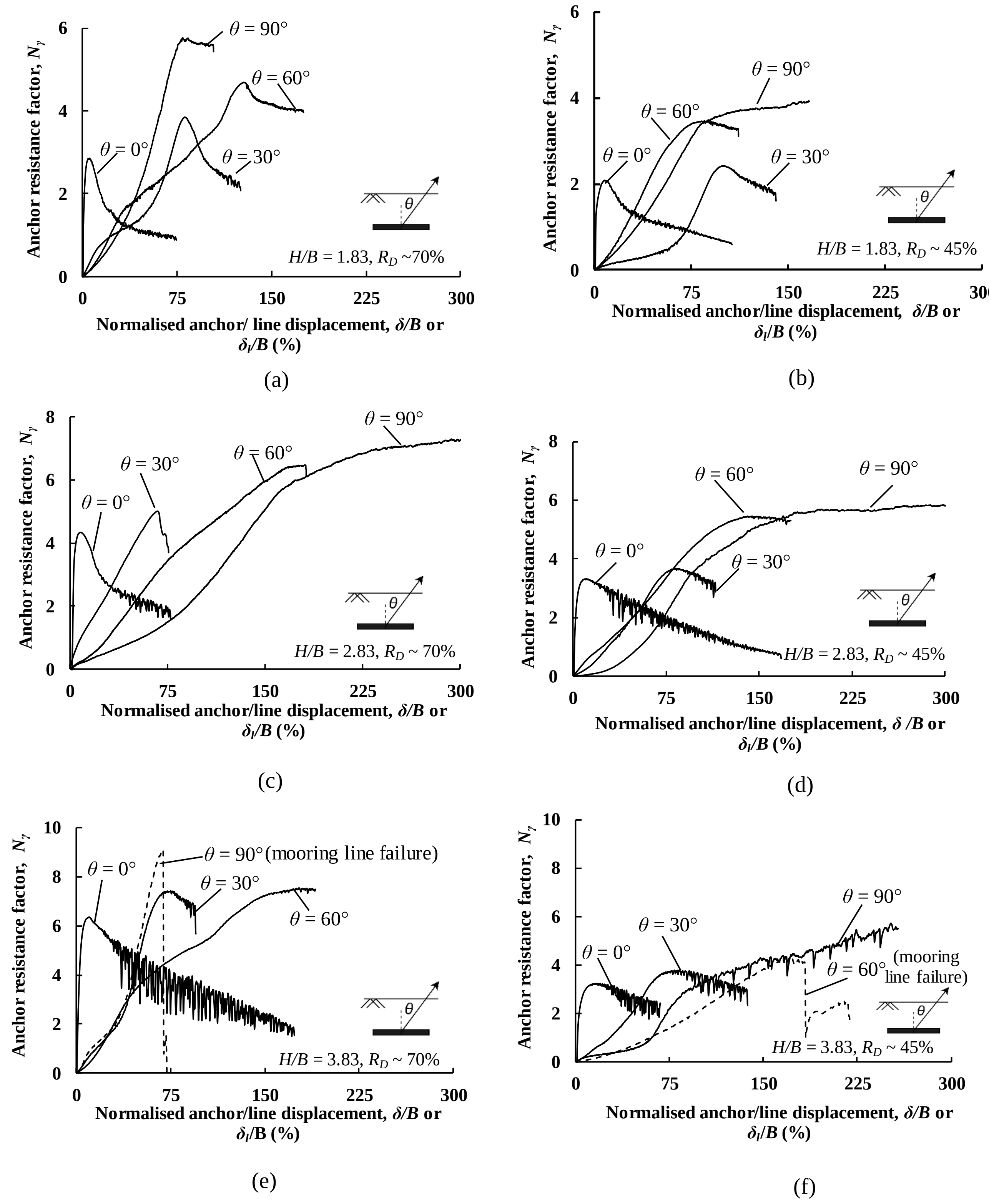

Fig. 6 : Normalised anchor capacity responses for: (a) H/B = 1.83 in dense sand, (b) H/B = 1.83 in loose sand, (c) H/B = 2.83 in dense sand, (d) H/B = 2.83 in loose sand, (e) H/B = 3.83 in dense sand, (f) H/B = 3.83 in loose sand

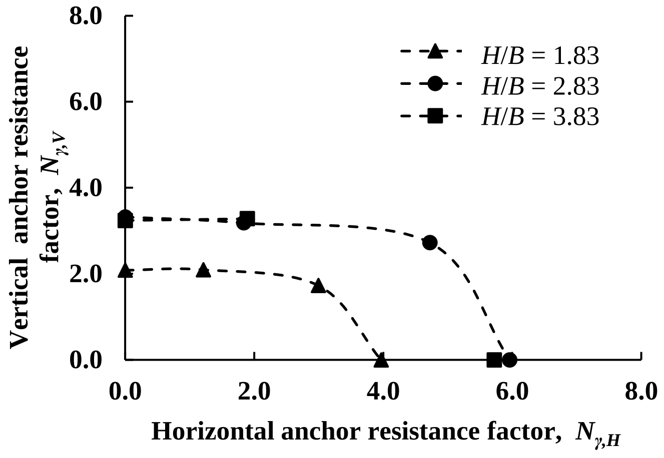

(a)

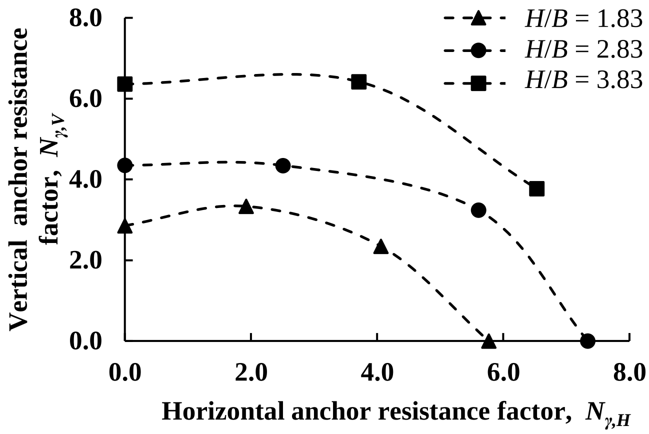

(b)

Fig. 7 : Interaction diagram of plate anchors at different embedment ratios in: (a) loose sand, (b) dense sand

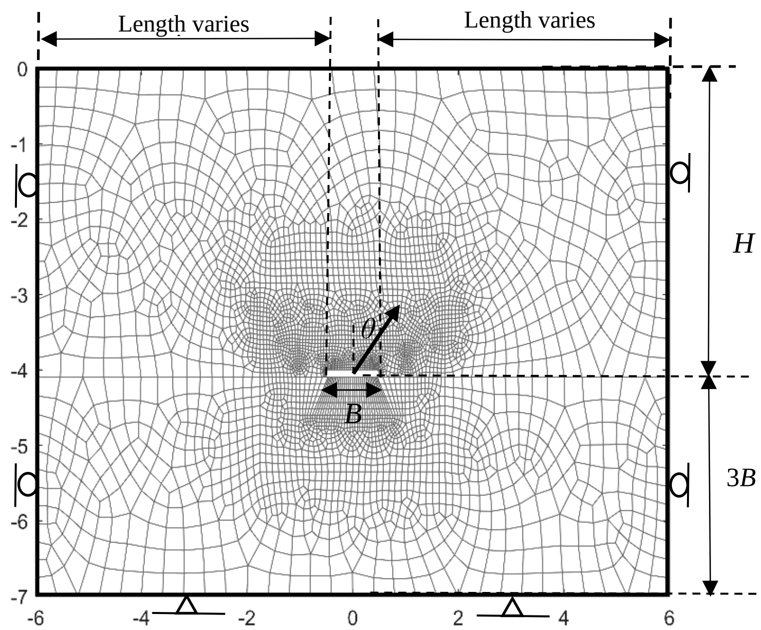

Fig. 8: Typical mesh details and boundary conditions for the anchor problem in Abaqus (H/B = 4)

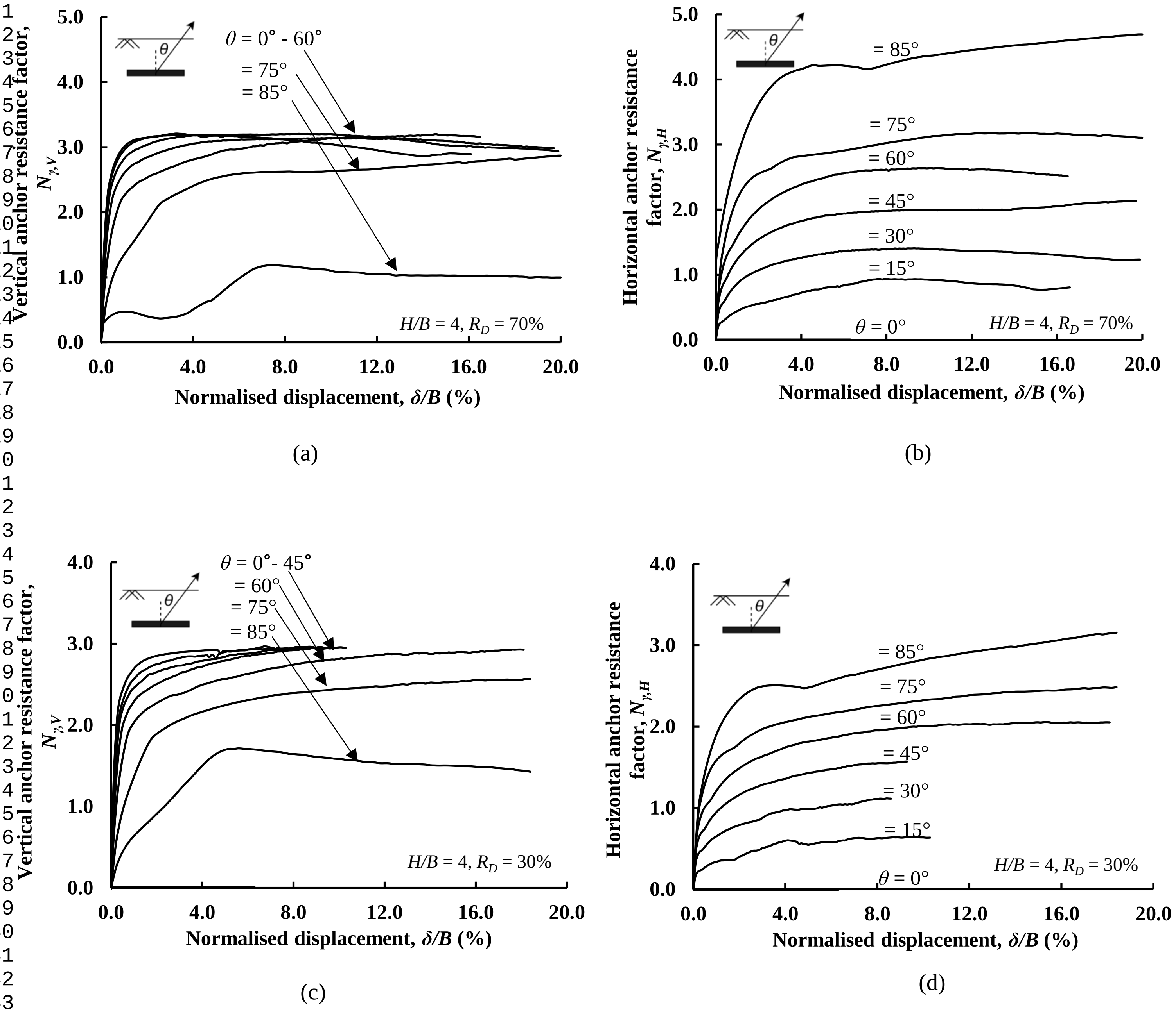

Fig. 9: Vertical and horizontal anchor resistance factors at different load inclinations at H/B = 4: (a) horizontal resistance in dense sand (R_D = 70%), (b) vertical resistance in dense sand (R_D = 70%), (c) horizontal resistance in loose sand (R_D = 30%), (d) vertical resistance in loose sand (R_D =30%)

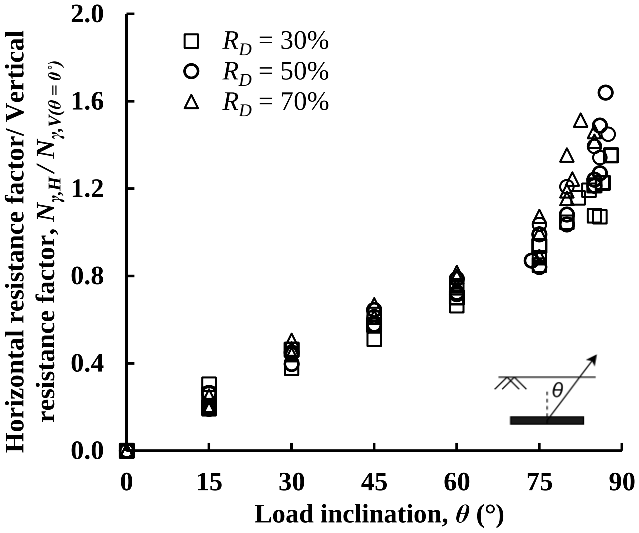

Fig. 10: Variation of peak normalised horizontal anchor factor with load inclination

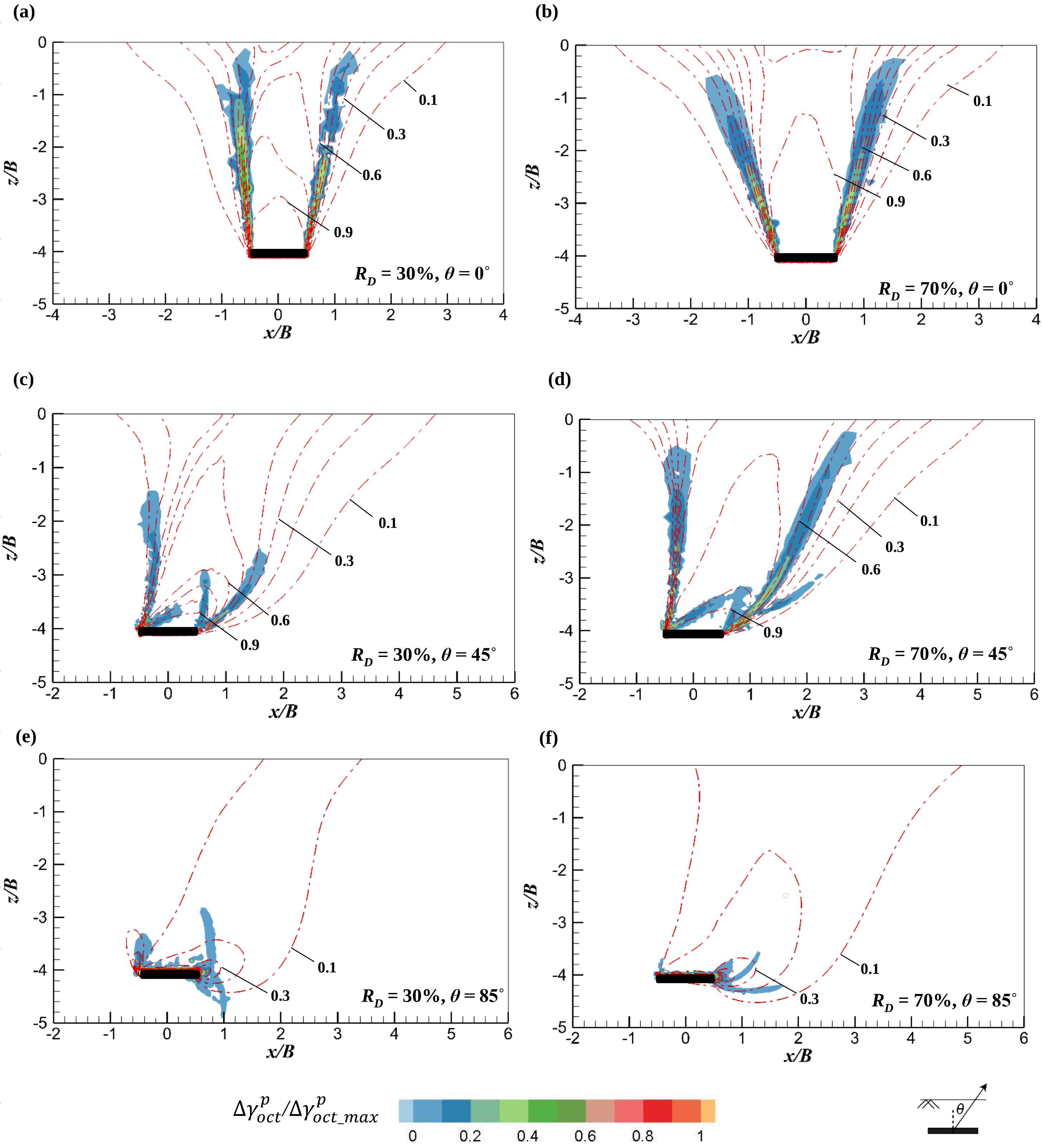

Fig. 11 : Numerically determined failure mechanisms at H/B = 4 compared against displacement contours (shown by red dashed lines)

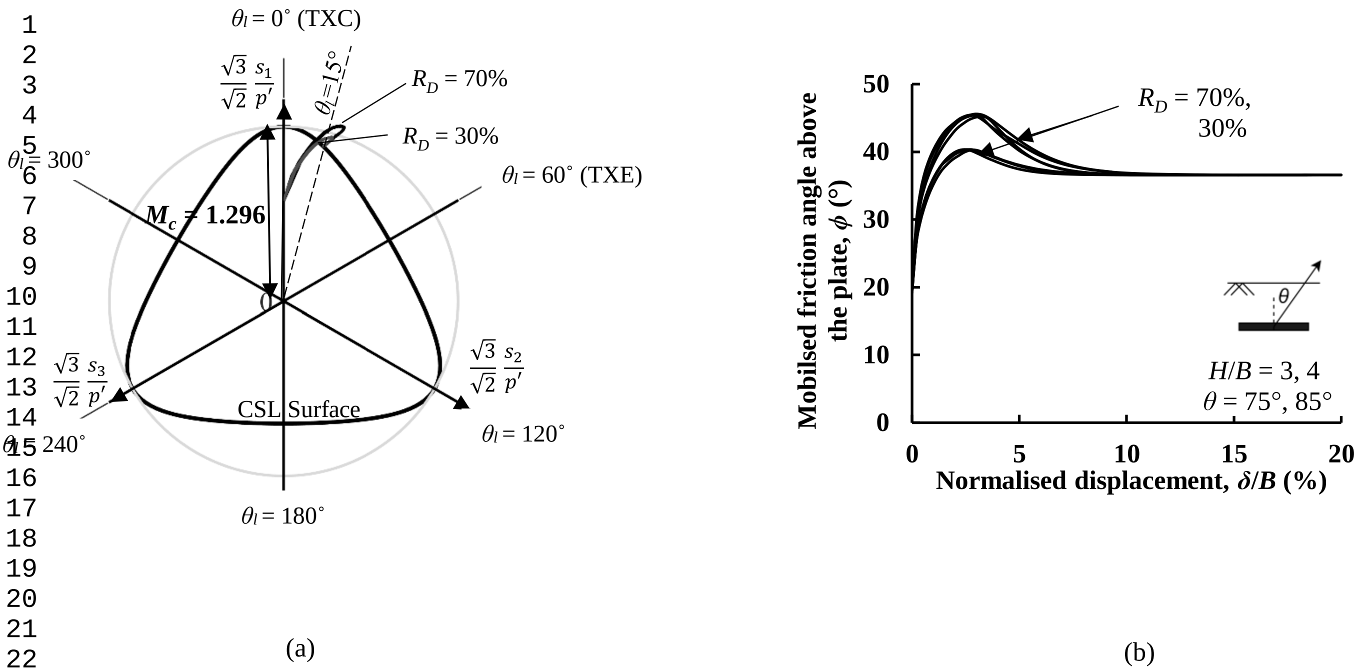

Fig. 12: Variation of (a) mobilised stress ratio M (= q/p') and (b) mobilised friction angle, ϕ for an element above the plate at an embedment ratio, H/B = 4 loaded at θ = 75° and 85° in loose and dense sand

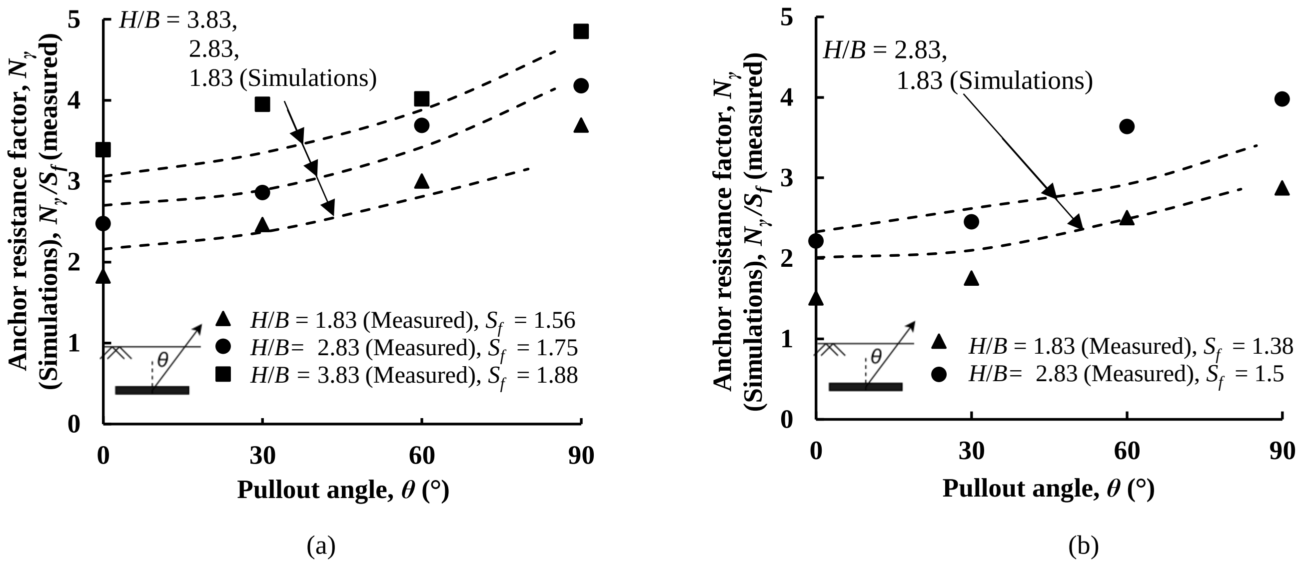

Fig. 13: Comparison of measured and simulated anchor capacity for different load inclinations and embedment ratios in: (a) dense sand (R_D = 70%) (b) loose sand (R_D = 40%)

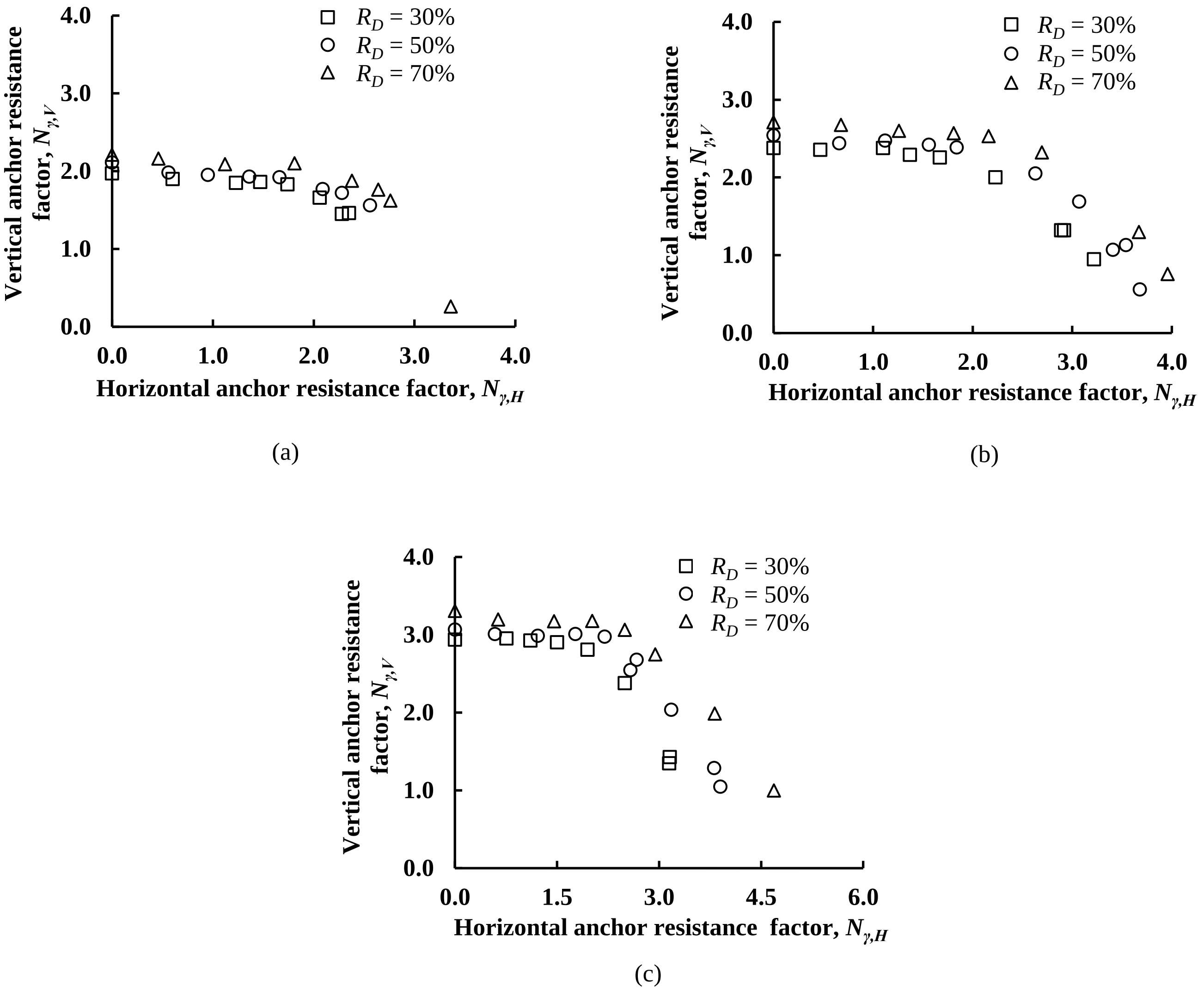

Fig. 14: Interaction diagrams for peak plate anchor capacity at: (a) H/B = 2, (b) H/B = 3, (c) H/B = 4

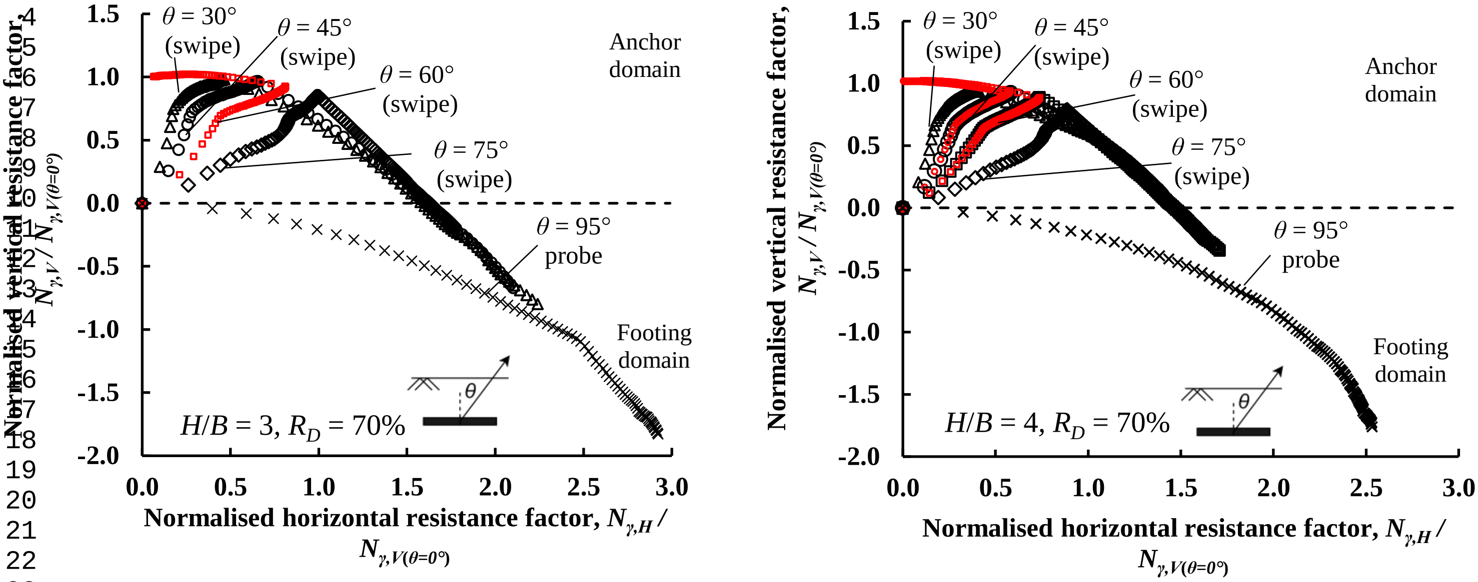

(a)

(b)

Fig. 15: Extended interaction diagrams from swipe analyses in dense sand at: (a) $H/B = 3$ (b) $H/B = 4$

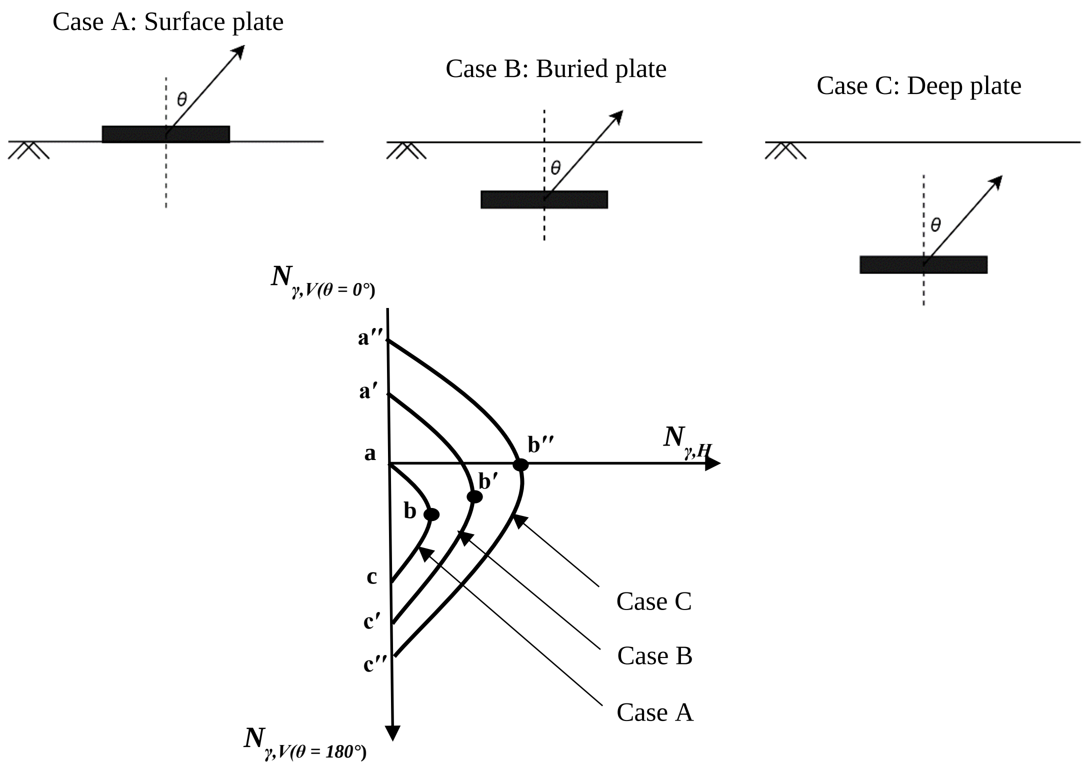

Fig. 16: Potential interaction diagrams for surface and embedded footings in sand

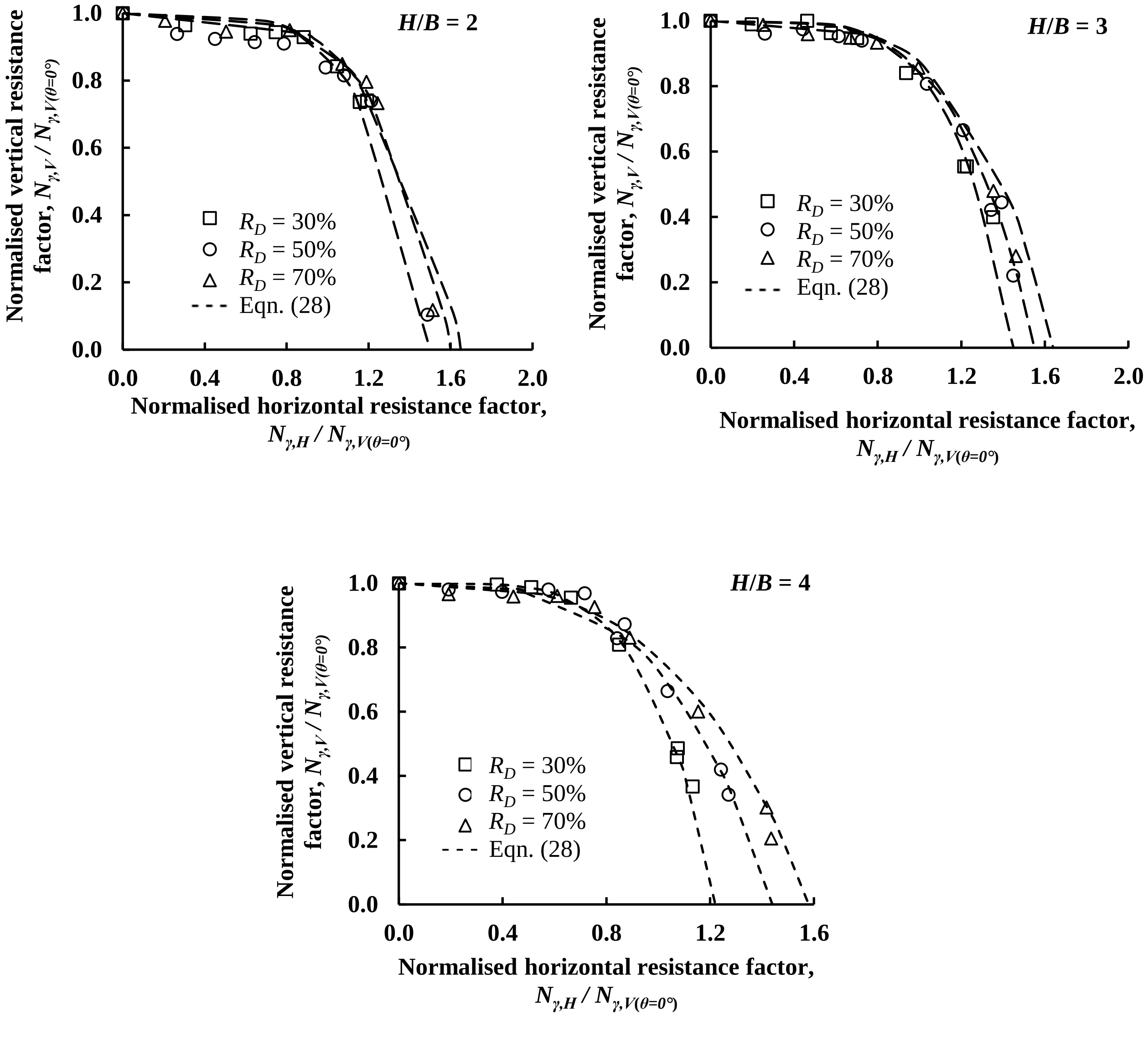

Fig. 17: Interaction diagrams for plate capacity at (a) H/B = 2, (b) H/B = 3, (c) H/B = 4